博士論文

Model Combining Fluid Hemodynamics and Fractal Theory for Analysis of *in vivo* Peripheral Pulmonary and Systemic Vascular Resistance of Shunt Cardiac Defects

（血流力学とフラクタル理論を用いた短絡型心疾患の in vivo 末梢体肺動脈血管抵抗のモデル解析と理論的考察）

中村　嘉宏

Contents

List of abbreviations **5**

Abstract **10**

1. Introduction **11**

1.1. Longitudinal distribution of the pressure gradient in the systemic circulation 11

1.2. Longitudinal distribution of the pressure gradient in the pulmonary circulation 12

1.3. The scale of precapillary arterioles 13

1.4. Pulmonary vascular disease in congenital cardiac defects 14

1.5. Radius exponent and fractal dimension 16

1.6. Murray's law and the relationship between blood flow and vessel radius 17

1.7. Introduction of fractal theory to the vascular tree 20

1.8. Systemic arterial tree and fractal dimension 23

1.9. Pulmonary arterial tree and fractal dimension 25

1.10. Change in fractal dimension in the pulmonary vascular disease 27

1.11. The aim of this study 29

2. Methods **31**

2.1. Physiological and pathophysiological premise 31

2.2. Fractal model to translate the q-r relationship of a single vessel into that of the whole vascular tree 33

2.2.1. Incorporating this branching fractal structure into the resistive arterial tree 36

2.2.2. Determination of x, A, and B 39

2.2.3. Estimation of n, β, γ, N_1, & N_w 40

2.3. Subjects 41

2.3.1. Subject data 41

2.3.2. Categorization of the patients with an L-R shunt 42

2.3.3. Estimation of the reversibility in the severe pulmonary hypertension 44

2.3.4. Cardiac catheterization and estimation of hemodynamics 45

2.4. Ethical procedures 47

3. Results **48**

3.1. Systemic circulation and the importance of body length in the new model 48

3.2. Application of this model to normal pulmonary circulation 52

3.3. Application to the pulmonary circulation with L-R shunt 52

4. Discussion **56**

4.1. Fractal dimension in peripheral systemic arteries 57

4.2. Fractal dimension in peripheral pulmonary arteries and with L-R shunt 58

4.3. Fractal parameters 59

4.4. Numbers of peripheral arterial vessels 63

4.4.1. Systemic arteries 63

4.4.2. Pulmonary arteries 63

4.4.3. Comparison of changes in the number and size of intra-acinar arteries due to L-R shunt between our prediction and histological data in the literature 64

4.5. Clinical benefits supposed by these changes in the pulmonary arterial system due to the L-R shunt 66

4.6. Verification of the ratio between $\Delta P_{prox\text{-}P}$ and $\Delta P_{peri\text{-}P}$ in our model analysis 67

4.7. Fåraeus-Lyndqvist effect: one of the non-Newtonian effects 69

4.8. Theoretical examinations of changes in x from around 2 to 3 70

4.8.1. The maximal blood flow hypothesis 70

4.8.2. The least energy principle 71

4.8.2.1. Energy function for an elastic artery 72

4.8.2.2. Energy function for a rigid artery 74

4.8.2.3. Verification of the least energy theory 76

4.9. Limitations 81

4.10. Conclusions 83

4.11. Appendix 85

5. Acknowledgements **87**

6. References **89**

List of abbreviations

Nominals

ao	Aorta
ASD	Arterial septal defect
BMP	Bone morphogenetic protein
CMA	Cremaster muscle artery
ECA	External carotid artery
F	Female
Ht	Hematocrit
L-R	Left-to-right
LPA	Left pulmonary artery
M	Male
PDA	Patent ductus arteriosus
PH	Pulmonary hypertension
PVD	Pulmonary vascular disease
PVR	Pulmonary vascular resistance
RPA	Right pulmonary artery
RBC	Red blood cell
R-L	Right-to-left
SCA	Subclavian artery
SD	Standard deviation
SMA	Superior mesenteric artery

TGF-β Transforming growth factor beta

VSD Ventricular septal defect

Functions and parameters in the model

α Exponent coefficient between vessel length and radius, defined by Eq. (38)

β Mean ratio of the mean radius of the k+1-th generation vessels to that of the k-th ones, defined by Eq. (11b); $0 < \beta < 1$

δ Ratio of r_t to r_n, equal to 0.429

ε Coefficient in the equation of the relationship between the blood flow and the vessel radius, defined in Eqs. (4) and (10)

γ Mean ratio of the mean length of the k+1-th generation vessels to that of the k-th ones, defined by Eq. (11c); $0 < \gamma < 1$

λ Coefficient for converting the resistance of cgs unit into mmHg·min/L in Eq. (12)

μ Fluid viscosity of the blood flowing in a vessel [cP (centipoise)]

$\mu(r)$ Fluid viscosity as a function of vessel radius in the Haynes' equation [cP], defined in Eq. (13)

μ_∞ Constant as the upper limit of viscosity in vessels of sufficiently large radii; equal to 4.0 [cP] in Eq. (13) of the Haynes' equation

ρ Specific gravity of blood [g/mL]

ζ Coefficient dependent on Reynolds number and L, defined by Eq. (48)

A Slope of ln-ln plot of Q against R_{peri}/BL, defined in Eqs. (19a) and (29)

B Intercept of ln-ln plot of Q against R_{peri}/BL, defined in Eqs. (19b) and (29)

BL Body length [m]

BSA Body surface area [m^2]

BW Body weight [kg]

C Cost function, defined by Eqs. (2) and (32) [J] and used in Murray's law

D Internal diameter of a vessel (i.e. $D = 2r$) [mm]

d_1 Ratio of l_1 to M

d_n Ratio of l_n to M, defined in Eq. (17)

E Energy function [J], defined by Eq. (31) and used in the least energy law

$G(n)$ Intermediary function structured by fractal parameters in Eq. (14b)

K Metabolic coefficient of blood flow and vessel wall [$J \cdot L^{-1} \cdot s^{-1}$] in Eqs. (2) and (37)

K' Proportional coefficient including the two elements of the equivalent metabolic energy of arterial oxygen volume and thermal energy in blood [$J \cdot L^{-1} \cdot s^{-1}$], defined in Eq. (36)

k Natural number from 1 to n

l Length of a vessel [mm]

l_1 Mean length of the 1st generation arteries [mm]

l_k Mean length of the k-th generation arteries [mm]

l_n Mean length of the n-th generation arteries [mm]

M Parameter of the body scale

N Mean ratio of the mean vessel number of $k+1$-th generation vessels to that of the k-th ones, defined by Eq. (11a)

N_1 Number of the 1st generation resistive arteries in the lung, given by Eq. (24) in this model

N_k Mean number of the k-th generation resistive arteries

N_n Mean number of the n-th generation resistive arteries

N_w Whole number of resistive arteries in the lung, quantified by Eq. (25)

n Natural number, representing the last generation of repetitively branched vessel

$\tilde{n}$ Mean real number estimated from the model analysis, given by Eq. (21)

P Mean pressure of a vessel [mmHg]

ΔP Loss of intravascular pressure [mmHg]

$P_{1st\text{-}pbr}$ Mean pressure between the two (left or right) pulmonary arterial branches [mmHg]

P_{ao} Mean pressure in the ascending aorta [mmHg]

P_{la} Mean pressure in the left atrium [mmHg]

P_{mpa} Mean pressure in the main pulmonary artery [mmHg]

P_{paw} Mean pressure of the pulmonary arterial wedge [mmHg]

$\Delta P_{1st\text{-}pbr}$ Pressure drop through the 1st pulmonary branching [mmHg]

$\Delta P_{cv\text{-}p}$ Pressure gradient through pulmonary capillaries and veins [mmHg]

$\Delta P_{peri\text{-}p}$ Pulmonary peripheral pressure gradient under $r \leq 100$ μm [mmHg]

$\Delta P_{peri\text{-}s}$ Peripheral systemic pressure gradient under $r \leq 100$ μm [mmHg]

$\Delta P_{prox\text{-}p}$ Proximal pulmonary pressure gradient under $r > 100$ μm [mmHg]

$\Delta P_{prox\text{-}s}$ Systemic proximal pressure gradient under $r > 100$ μm [mmHg]

Q Blood flow through a total vascular network [L/min]

Q_p Pulmonary blood flow [L/min]

Q_s Systemic blood flow [L/min]

Q_p/Q_s Ratio of pulmonary to systemic blood flow

q Blood flow of a blood vessel [L/min]

q_k Mean blood flow of the k-th generation arteries [L/min]

q_n Mean blood flow of the n-th generation artery [L/min]

$q(r)$ Blood flow as a function of radius in Eq. (30)

R_{cyl}	Vascular resistance of a rigid circular cylinder [mmHg/L/min], defined in Eq. (1) by Hagen–Poiseuille's equation
Re	Reynolds number, defined by Eq. (47)
R_{peri}	Peripheral arterial resistance [mmHg/L/min]
$R_{peri\text{-}p}$	Peripheral pulmonary arterial resistance [mmHg/L/min]
$R_{peri\text{-}s}$	Peripheral systemic arterial resistance [mmHg/L/min]
r	Inner radius of a vessel [μm or mm]
r_1	Mean radius of the 1st generation arteries, set at 100 μm in this model
r_k	Mean radius of the k-th generation arteries [μm]
r_n	Mean radius of the n-th generation arteries, set at 10 μm in this model [μm]
r_t	Constant equal to 4.29 [μm] in the Haynes' equation in Eq. (13)
U_K	Kinetic energy of blood flow, defined by Eq. (33) [J]
U_M	Metabolic and thermal energy of blood flow, defined by Eq. (36) [J]
U_P	Pressure energy of blood flow, defined by Eq. (34) [J]
ΔU_K	Loss of kinetic energy of blood flow [J]
ΔU_M	Loss of metabolic and thermal energy of blood flow [J], defined in Eqs. (2) and (37)
ΔU_P	Loss of pressure energy of blood flow [J], defined by Eq. (35)
v	Linear velocity at the gravitational center of blood flow [m/s]
x	Radius exponent defined by Eq. (10), corresponding to the fractal dimension
x_p	Fractal dimension of the pulmonary arterial tree
x_s	Fractal dimension of the systemic arterial tree

Abstract

The fractal state of the arterial vascular tree is considered to have a universal dimension related to the principle of minimum work rate, but can demonstrate the capacity to adapt to other dimensions in disease states such as congenital high-flow pulmonary hypertension (PH) by a process that is not completely understood. To document and interpret fractal adaptation in patients with different degrees of PH, pulmonary and systemic vascular resistance was analyzed using a model that evaluated the fractal dimension, x, of the Poiseuille resistance contribution of the arterial vessel radius between 10 and 100 μm, via the proportionality $Q \propto (R_{peri}/BL)^{-x/4}$, with Q, R_{peri}, and BL clinically observed variables representing total pulmonary or systemic blood flow, its peripheral arterial resistance, and body length, respectively. Identification of x in the pulmonary (p) and systemic (s) beds was evaluated using hemodynamic data of 213 patients, categorized into 7 groups by PH grade. In controls without PH, $x_p = 2.2$ while the dimension increased to 3.0, with the systemic dimension constant at $x_s = 3.1$. Our model predicts that severe grades of PH are associated with: more elongated and hindered vessels in the periphery, and reductions in vessel numbers, as unit pulmonary resistive arterial trees (N_1) and their component intra-acinar arteries (N_w). These model network changes suggest a complex adaptive process of arterial network reorganization in the pulmonary circulation to minimize the work rate of high-flow congenital heart defects.

1. Introduction

The whole vascular system, pulmonary or systemic, can be divided into three segments longitudinally, comprising the proximal large arteries, peripheral resistive arteries, and capillaries and veins [24, 66]. Hereafter, suffixes p and s stand for pulmonary and systemic, respectively.

1.1. Longitudinal distribution of the pressure gradient in the systemic circulation

In the systemic circulation, it is generally estimated that the mean pressure in the ascending aorta (P_{ao}) drops 10% in large arteries with $r_s > 100$ μm, which function as an elastic reservoir or a Windkessel [59, 66], 60% in small resistive arteries with $r_s \leq 100$ μm, and the remaining 30% in capillaries and veins [66].

Mean aortic blood pressure falls only 2% from the ascending aorta to small arteries whose inner radius (r) narrows to approximately 1 mm [79] (or 2.5 mm [66]) in the human systemic circulation [66]. The sufficient elasticity and resultant large distensibility in proximal systemic arteries are due to the large ratio of constituent elastin over collagen and the thin smooth muscle layer [21, 66].

By contrast, as much as 60% of mean aortic blood pressure is lost in the peripheral systemic resistive arteries ($0.04 \leq r_s \leq 0.1$ mm) [66]. A much smaller elastin/collagen ratio in more peripheral systemic arteries renders their wall a lot stiffer [18, 49, 66, 79]. Furthermore, adding a thick smooth muscle layer to this already stiffer walls property makes the change in the radius in response to internal pulsatile pressure alteration extremely small in systemic arterioles [58, 66].

Some histologists, however, advocate another intermediate category of systemic arteries around $0.1 < r_s \leq 1$ mm [79] (or ≤ 2.5 mm [66]), where the pressure gradient comprises 8% of mean aortic pressure in humans [66]. They describe these arteries as elastic-muscular and their wall properties lie in between the more proximal elastic and more peripheral resistive arteries [66, 78].

1.2. Longitudinal distribution of the pressure gradient in the pulmonary circulation

Hakim et al. (1982) described that the trans-pulmonary pressure drop can be divided into the three segments through *in situ* experiments with perfused canine lungs by arterial and venous occlusion: the middle non-muscular, much more distensible fraction contributing a major fraction of the vascular compliance, relatively non-distensible muscular arteries, and similarly non-distensible veins [24].

Brody et al. estimated the longitudinal distribution of vascular resistance as being 46% arterial, 34% capillary, and 20% venous [7]. Bhattacharya et al. reported the distribution of resistance as 5.4% in pulmonary arteries with diameters > 50 μm, 32.1% in those of diameters of 10–50 μm, and 62.5% in capillaries and veins by the direct measurement in the isolated perfused dog lungs [6]. In the physiological pulmonary circulation, normal pressure through the pulmonary capillaries and veins ($\Delta P_{cv\text{-}p}$) is reported to be larger than in its systemic counterpart, amounting to approximately 50% of the total transpulmonary pressure drop in canine isolated perfused lungs [6, 7, 24, 59, 71].

The normal pulmonary arterial circulation shares 50% [6, 24, 59] of the whole mean transpulmonary pressure gradient, which is as low as 6–7 mmHg in humans [14, 46, 66]. The mean pressure gradient through them amounts to only 3.3 ± 0.6 mmHg [63], as estimated in controls of our clinical data in this study as shown later. The pulmonary arterial wall is much thinner, less or non-muscularized, and more distensible than its systemic counterpart [1, 11, 23, 61, 66] even though peripheral pulmonary arteries of $r_p \leq 0.1$ mm comprise the most resistive in the pulmonary arterial circulation [6, 59].

1.3. The scale of precapillary arterioles

The radius of the terminal arteriole is reported to be around 7–10 μm in in vivo rat's systemic [35, 53], canine systemic [75] and pulmonary [12], and human systemic [80] and pulmonary [36] arteries, because the radii of terminal arterioles are similar in spite of being from different mammalian species. These data suggest that the scale of red blood cells (RBCs), whose diameter is around 7 μm, is critical to determine the radius of terminal arterioles as well as that of capillaries (5 μm) [53, 66, 77].

1.4. Pulmonary vascular disease (PVD) in congenital cardiac defects

A certain category of congenital cardiac defects is characterized by augmented pulmonary blood flow, which is called a left-to-right (L-R) shunt defect. The most common three defects are atrial septal defect (ASD), ventricular septal defect (VSD), patent ductus arteriosus (PDA), and their combination. It is well-known that they develop secondary pulmonary vascular disease (PVD) mainly on the arterial side of the peripheral pulmonary vascular bed over time as a reactive adjustment to the augmented shunt flow and pulmonary hypertension (PH) [4, 25, 27, 31, 32, 37, 59, 69].

The reversible pathological changes in CHD with PH is characterized by medial hypertrophy of pre-acinar vessels and muscularization of normally non-muscularized arterioles [27, 31, 59, 69, 70, 83, 84]. These may be accompanied by mild proliferation of intimal cells. In the early days when When Wagenvoort [84], and Heath & Edwards [27] published their studies around 1960, they considered that the secondary PH due to L-R shunt might be reversible when the histology showed medial hypertrophy alone. Medial hypertrophy is also observed in all healthy newborns after birth, reversing in the first 8 weeks of life in fact [83]. However, children with VSD were reported to often display the heterogeneity and variability partially maintaining proliferative intimal changes within 1 year, and even plexiform lesions within 2.5 years after birth [83, 84]. Therefore, the irreversible form of PVD will progress much later to its final stage of further intimal proliferation, fibrosis, plexiform lesion, and arteritis without surgical intervention [27, 31, 59, 69, 70, 83, 84].

These features and their progression were first reported and classified into 6 grades of structural changes in the pulmonary arteries with reference to congenital cardiac septal defects by Heath & Edwards in 1958 [31, 59, 69, 70, 83]. In their review article, Van der Feen et al. explained the mechanism of PVD as follows [83]. Blood flow is originally laminar in the normal pulmonary circulation. In the situation of a large L-R shunt, increased blood flow and pressure makes

turbulence in the arteries, especially at their branch points. Turbulence causes endothelial dysfunction, which induces medial hypertrophy together with increased pressure. Turbulence also disturbs the balance between transforming growth factor beta (TGF-β) vs. bone morphogenetic protein (BMP) [20], which elevates apoptosis, proliferation, and inflammation. Misbalance in these sequences triggers the endothelial proliferation, which may become resistant to apoptosis and create a neointimal layer. The neointimal layer makes the arterial inner surface irregular, increases the disruption of flow patterns, and further disturbs signaling balances. An irreversible vicious cycle is produced in series by this mechanism [83].

It is also widely agreed that this early stage of PVD in large defects results from both reflexive and neurohumorally mediated vasoconstriction by the above mentioned increased smooth muscle layer toward the peripheral small arteries and arterioles [27, 31, 37, 59, 69]. Congenital L-R shunt defects thus induce medial hypertrophy and vasoconstriction of intra-acinar arteries ($0.004 \leq r_p \leq 0.1$ mm) with secondary PH a few months after birth along the postnatal course of the disease [17, 27, 31, 59]. Both of these pathophysiological changes are considered to induce strikingly decreased elasticity and increased rigidity of intra-acinar arterial wall properties.

In addition to the vasoconstriction, the quantitative alveolar-to-arterial ratio is reported to fall in these pediatric patients, because the normal or extended growth of intra-acinar arteries becomes disturbed and substantially interrupted [27, 31, 69, 70, 83, 84]. It is not yet well explained what mechanisms hamper the development of intra-acinar arteries in these patients. [83, 84].

1.5. Radius exponent and fractal dimension

Biological vessel structures have been simulated by fractal theory [3, 12, 15, 17, 19, 39, 41, 44, 48, 50, 55, 80, 86, 87, 94], and the fractal dimension provides us with biologically important meanings of the branching pattern governing a tree-like structure and its space-occupying rules [55, 87]. The fractal dimension was revealed as 3 in the branching pattern of arteries in organs [35, 41, 48, 57, 72, 75, 80] and of bronchi in the lung [44]. The fractal dimension of $x = 3$ in bifurcating peripheral resistive systemic arteries was reported to be by morphometric studies [41, 48] as well as flow-radius measurement *in vivo* [35, 53, 57].

Murray's law is well known as the minimum work theory to explain the ideal radius exponent equal to 3 [62]. The radial cubic law in organ vasculatures was also theoretically accounted for by the uniform pressure distribution [15] and optimal space-filling of fractal [55].

1.6. Murray's law and the relationship between blood flow and vessel radius

Murray (1926) theoretically predicted the existence of 'optimality principle' in the relationship between the blood flow through a cylindrical vessel and the vessel radius (Fig. 1) [62].

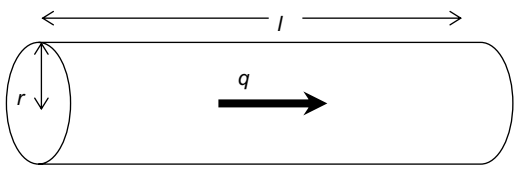

Figure 1. A single tubular vessel model cited from ref. [64]. Blood flow (q) flows through the vessel whose radius and length are represented by r and l, respectively. q is defined as volume blood flow per unit time.

The vascular resistance R_{cyl} of a cylindrical vessel is given in equation (1) as Hagen–Poiseuille's equation when we hypothesized the vessel as a rigid one, with blood viscosity, radius, and length as μ, r, and l, respectively [12, 15, 48, 57, 62, 66, 75].

$$R_{\text{cyl}} = \frac{8\mu l}{\pi r^4} \tag{1}$$

With the volume blood flow rate per unit time, the metabolic rate of blood [48, 62] as well as vessel wall [57] per unit time volume, and cost function representing the lost energy per unit time to transport the blood flow through the vessel as q, K, and C, respectively, the equation was designed as follows [15, 48, 57, 62, 75]:

$$C = \left(\frac{8\mu l}{\pi r^4}\right) q^2 + K\pi r^2 l. \tag{2}$$

After C was partially differentiated with respect to r, $\partial C/\partial r = 0$ resulted in [15, 48, 57, 62, 75]:

$$q = \varepsilon r^3, \text{ where } \varepsilon = \frac{\pi}{4}\sqrt{\frac{K}{\mu}}. \tag{3}$$

Thus the predicted relationship between q and r indicated by Eq. (3) must be selected and adopted in the

living body because this condition guarantees the minimum work requirement, under which q is regulated and maintained proportionally to r^3 (Fig. 2).

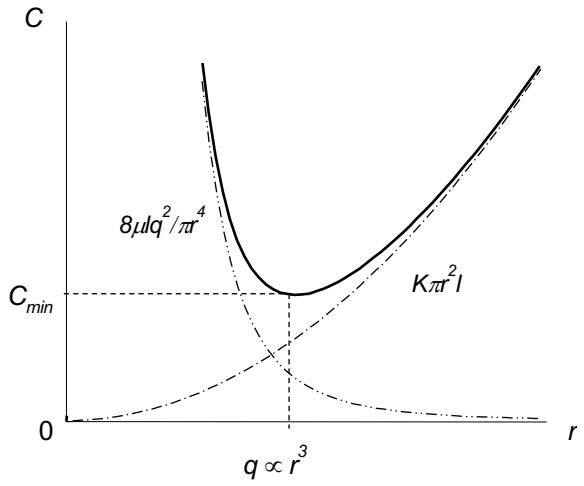

Figure 2. Graph of minimum work theory designed by Murray (1926) [62]. $C_{\min}$ represents the minimum energy cost per unit time; μ, blood viscosity; q, r, and l, the blood flow, the vessel diameter, and the vessel length, respectively. $8\mu lq^2/\pi r^4$ and $K\pi r^2 l$ are presented in equation (2). The point of $C_{\min}$ is given in the condition with $q \propto r^3$ by partial differentiation of C with respect to r. Figure 2 was cited from ref. [64].

Murray's law can be interpreted as the ideal model of vessel branching [15, 48, 41, 72, 74, 75, 82]. When a mother vessel with her radius r_{M} branches into two daughter vessels with radii r_{D1} and r_{D2} ($r_{\mathrm{D1}} > r_{\mathrm{D2}}$), with q_{M}, q_{D1}, and q_{D2} as their blood flow through them, respectively (Fig. 3), the common K in Eq. (3) gives:

$$q_{\mathrm{M}} = \varepsilon r_{\mathrm{M}}^3, q_{\mathrm{D1}} = \varepsilon r_{\mathrm{D1}}^3, \text{and } q_{\mathrm{D2}} = \varepsilon r_{\mathrm{D2}}^3. \tag{4}$$

As the sum of blood flow through branching is preserved as:

$$q_{\mathrm{M}} = q_{\mathrm{D1}} + q_{\mathrm{D2}}, \tag{5}$$

Eqs. (4) and (5) ensures:

$$r_{\mathrm{M}}^3 = r_{\mathrm{D1}}^3 + r_{\mathrm{D2}}^3. \tag{6}$$

When repeated branching succeeds under this condition through the whole vascular tree, the

fractal dimension is also regarded as 3, as described at the next section.

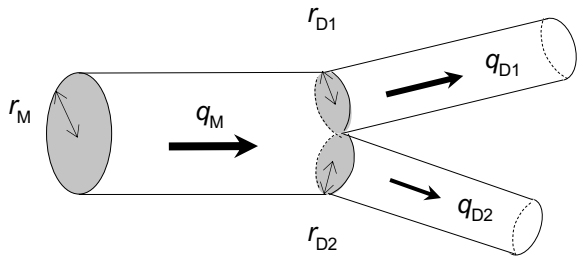

Figure 3. The branching model from the mother to two daughter vessels. q_M, and r_M represent the blood flow rate and radius of the mother, respectively, suffixed with $_M$; those of daughters 1 and 2 are presented with suffixes $_{D1}$ and $_{D2}$, respectively. Figure 3 was cited from ref. [64].

The shear-stress (τ) on the internal surface of the vessel wall is measurable as $4\mu q/\pi r^3$ [40, 41, 74, 85], which is well known as an agent that affects and regulates vessel radius [83]. Because τ of three vessels is written by Eq. (4) as:

$$\tau = \frac{4\mu q_M}{\pi r_M^3} = \frac{4\mu q_{D1}}{\pi r_{D1}^3} = \frac{4\mu q_{D2}}{\pi r_{D2}^3}, \quad (7)$$

Murray's law also gives the background of the uniform shear-stress theory at the same time [40, 41, 74, 85].

1.7. Introduction of fractal theory to vascular tree

Mandelbrot (1983) reported the mathematical characteristics based on self-similarity in geometric structures of seashore lines and rivers, or in morphology of tree branching, where their self-similarity is described with fractal parameters and functions [55]. After his work this concept of a fractal pattern has been developed and become well known worldwide. Many researchers also reported the presence of fractal structures in such living objects as bronchial branching [44] and vascular network [3, 17, 41, 57, 66] as described above.

When we suppose that every k-th generation vessel with mean radius r_k branches into N vessels on the average of the k+1-th generation with radii r_{k+1} through the vascular tree, letting k and N be two natural numbers, the fractal model is written by using a real number x as:

$$r_k^x = N r_{k+1}^x. \tag{8}$$

In the fractal structure, vessels undergo successive branching through generations of the vascular tree obeying Eq. (8). When $N = 2$ and $x = 3$, Eq. (8) results in Eq. (6). Letting q_k and q_{k+1} be mean blood flow through a single vessel of k-th and k+1-th generation, respectively, preserved blood flow is written as:

$$q_k = N q_{k+1}. \tag{9}$$

Eqs. (8) and (9) yield the next equation similar to Eq. (4) with the fractal dimension x as:

$$q_k = \varepsilon r_k^x$$

This can be written more generally as:

$$q = \varepsilon r^x \tag{10}$$

[3, 34, 35, 57, 88], where x is also called the radius exponent [39, 55] or the junction exponent [3, 48], and corresponds to the fractal dimension of embedding in fractal theory for an asymmetric vascular tree applicable to multiple consecutive arterial generations [3, 15, 39, 50, 55, 80, 87, 94].

In normal physiological situations, the mean of x stayed between 2.0 and 3.0, although its range was reported to be from as low as 1.0 to over 4.0 through various methods in a variety of mammalian arteries [3, 12, 34, 41, 48, 53, 57, 75, 80, 88, 94] as partially indicated in Figures 4A and 4B.

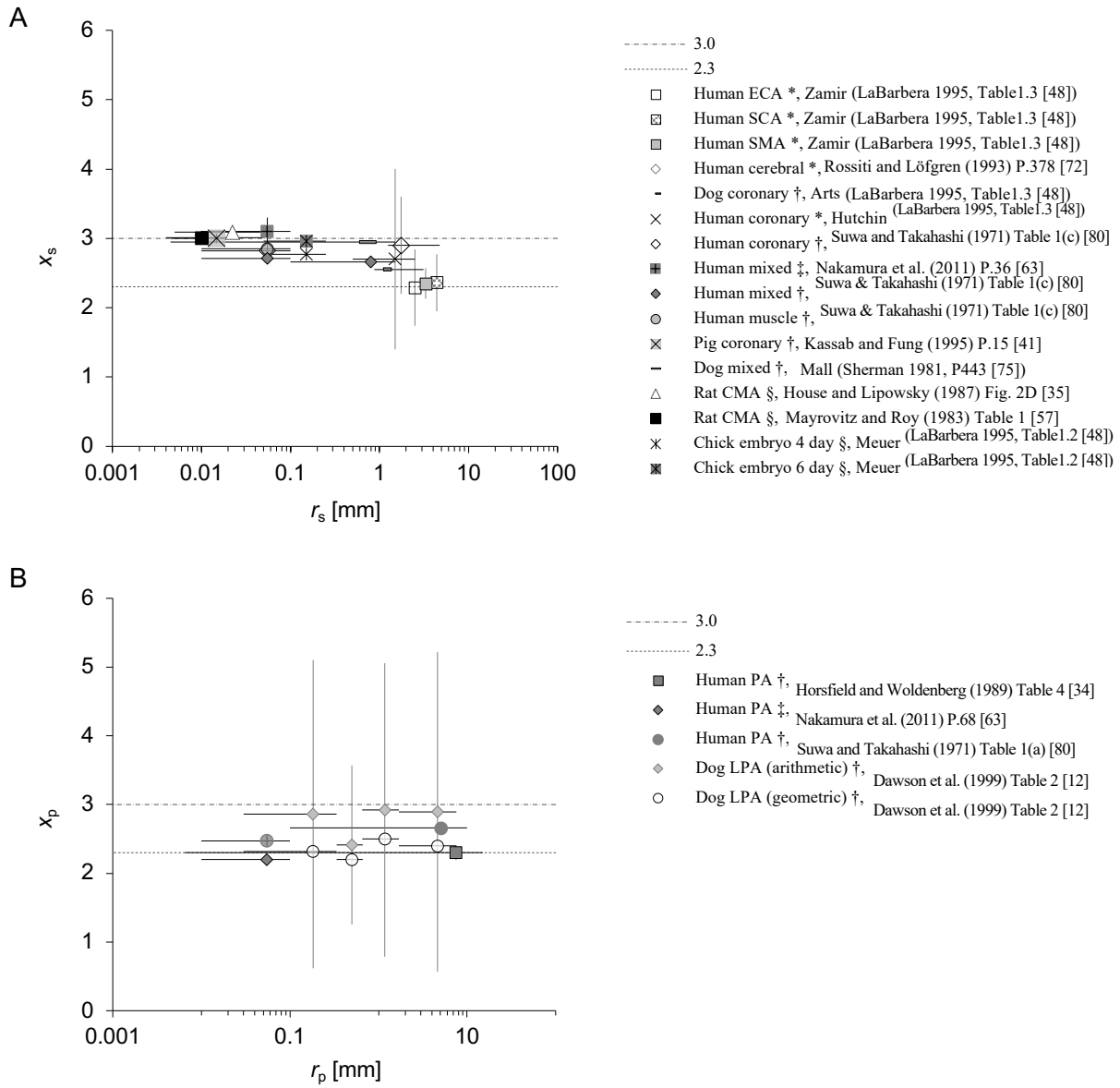

Figure 4. A. Distribution of reported x_s in a variety of animals from previous studies using various methods, all of which, except for Meuer's data [48], are humans [48, 63, 72, 80] and mammals [35, 41, 48, 57, 75]. CMA, ECA, SCA, and SMA indicate the cremaster muscle, external carotid, subclavian, and superior mesenteric arteries, respectively. The radii of ECA, SCA, and SMA were estimated from Table 1 in Olufsen et al. [67] as 2.5 mm, 4.4 mm, and 3.3 mm, respectively; the radius of ECA was tentatively substituted for the mean of the minimal radius at the outlet of bilateral common carotid arteries. The results from House and Lipowsky [35] presented in this figure were derived from the volumetric flow of red blood cells. **B.** Distribution of reported x_p in humans [34, 63, 80] and dogs [12]. PA, pulmonary arterial tree; LPA, left pulmonary artery. r, vessel radius, presented at the mid-point with the range because the mean and median were not reported in the literature; x, radius exponent, defined by in Eqs. (9) or (10) and presented as the mean with one standard deviation. Suffixes s and p indicate systemic and pulmonary. Methodology is indicated by symbols: *, angiography; †, cast-morphometry; ‡, model analysis with catheter data; §, direct measurement *in vivo*. Figure 4 was cited from ref. [65] after modification.

1.8. Systemic arterial tree and fractal dimension

Previously reported results of x_s were plotted in Figure 4A against the corresponding r_s, for which we were able to identify the range. These data mainly reflect r_s-x_s sets listed in the review article by LaBarbera' [48], and include those reported by other studies [34, 35, 41, 57, 63, 72, 75, 80].

$x_s \approx 2.0$–2.3 was reported by angiographic morphometry in proximal systemic arterial branching structures, such as from the aorta to next-generation large arteries [42, 48, 93, 94], where little pressure drop takes place. Meanwhile, transitional or intermediate values of $x_s \approx 2.7$ have also been observed in several organs of some mammalian systemic arteries [3, 48, 80].

In contrast, $x_s \approx 3$ has consistently been reported in peripheral systemic resistive arteries of $0.004 \leq r_s \leq 0.1$ mm [66] by postmortem cast-morphometry in mammals [41, 75] and direct measurement of the q_s-r_s relationship in *in vivo* rat cremaster arteries [35, 57]. In general, it has been accepted that at least the systemic vasculature in regional circulation is regulated and maintained at $x \approx 3$ [15, 35, 57].

To date, as mentioned above, the most influential and prevailing theory for $x_s = 3$ found in the peripheral systemic arterial bed [41, 48, 72, 75, 82, 92] is Murray's law, which applied the minimum cost principle to a rigid cylindrical artery with viscous Newtonian steady flow [15, 21, 48, 57, 62, 75, 82]. Fractal space-filling embedding [15, 55] also provides an alternative theoretical basis for $x_s = 3$. However, these two principles are not by themselves effective enough to explain the consistency of the radius exponent of the proximal systemic large arteries originating directly from aorta [42, 75, 92], proximal systemic ($r_s > 1$ (or 2.5) mm) [48, 92, 93], or intermediate systemic elastic-muscular arteries ($0.1 < r_s \leq 1$ (or 2.5) mm) [48, 80], of course including the pulmonary arterial beds, on the common basis [65].

Several explanations for x from 2.0 to 2.7 have since been attempted, such as the cross-sectional area-preserving law ($x = 2.0$) [3, 45, 87, 88, 93], minimization of both drag and power loss ($x = 2.0$) [3, 21], complete turbulence ($x = 7/3 = 2.33$) [3, 82], minimization of surface area and power loss ($x = 2.5$)

[3, 21], and minimum volume principle ($2.1 < x < 2.8$) [3, 88].

Hagen–Poiseuille's equation has long been used universally to express the pressure gradient in arterial models including Murray's theory, irrespective of whether r is derived from big arteries such as the aorta or from small peripheral arterioles [12, 15, 17, 39, 41, 42, 45, 48, 57, 62-66, 72, 75, 80, 82, 87, 92]. However, it is also well known that Hagen–Poiseuille's equation is unable to accurately estimate vascular resistance in proximal systemic elastic arteries and whole pulmonary arteries because of their large pulsatile fluctuation of radius [34, 60, 66]. On the other hand, Bernoulli's equation can and should rather reasonably be applied to blood flow through elastic arteries, such as proximal human systemic or whole pulmonary arteries [5, 51, 52, 66].

1.9. Pulmonary arterial tree and fractal dimension

Figure 4B presents the pulmonary arterial counterpart reported in humans and dogs in the literature [12, 34, 63, 80]. Mean x_p was reported to be 2.3 ± 0.1 ($0.0065 \leq r_p \leq 15$ mm) [34], or to range from 2.47 ± 0.09 ($r_p < 0.1$ mm) to 2.66 ± 0.07 ($r_p \geq 0.1$ mm) by pulmonary arterial cast-morphometry of normal humans [80]. The relationship between q_p and r_p in the human pulmonary arterial tree simulated by Singhal et al. on the basis of their cast-morphometry [76] is also presented with a ln-ln plot in Figure 5, where the slope of this plot clearly indicates that x_p stays constant at 2.32 starting from proximal large to peripheral small arteries.

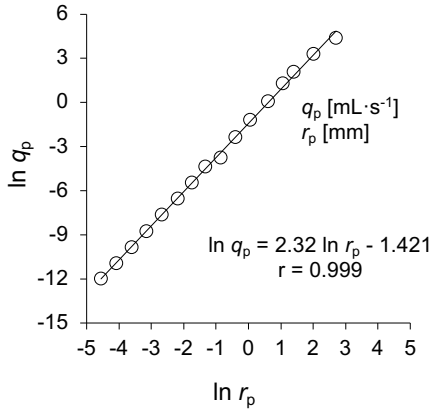

Figure 5. Ln-ln plot of human pulmonary arterial blood flow (q_p) in a vessel against its corresponding vessel radius (r_p). The original data for the plot are derived from combining Tables 4 and 5 from Singhal et al. [76] in the condition with an assumed cardiac output of 4.8 L/min in a 32-year-old female human. The slope of this proportionality is equal to radius exponent x. r indicates the correlation coefficient. Figure 5 was cited from ref. [65].

Cross-sectional area preservation at each branching, $x_p \approx 2$ functionally suggests that constant linear blood flow velocity is maintained there. This may be advantageous in transporting blood in a low pressure gradient, because no kinetic energy is lost at ramifications. Structurally, $x_p \approx 2$ also implies that the peripheral arterial ramification pattern is short of the space-filling embedding in the lung [15, 55], whereas the bronchial branching pattern has been reported to indicate $x = 3$ [44]. The trait of space-filling embedding of airways in spite of the arterial tree design is suggesting that long-term natural selection seems to have given priority to the optimal structure for gas exchange more than that of blood distribution within a given space in the lung.

Horsfield and Woldenberg reported $x_p = 2.3 \pm 0.1$ at 1,937 bifurcations of human whole pulmonary arterial trees as an *in vitro* morphometric result using resin casts from two fully inflated human lungs, counting from the main pulmonary artery down to terminal arterioles [34].

The heterogeneity of x_p from 2 to 3 was also reported in whole pulmonary arterial trees of human [88] and dogs [12, 40]. A marked large standard deviation (SD) of the arithmetic mean of x_p around 2.9 was described in canine lungs using a cast-morphometric study by Dawson et al. [12], as indicated in Figure 4B. Karau et al. reported that exponent x_p in a vascular bifurcation is heterogeneous from 2 to 3 in the pulmonary arteries on the basis of X-ray morphometry of isolated perfused canine lungs [40]. Woldenberg (1983) tried to explain the variety of human x_p from 1 to 3 separately by multiple cost factors [88].

In fact, multifractility [19, 55, 94] exists in either systemic and pulmonary vasculatures in mammals [19, 94], where the fractal characteristics may vary at different levels of radii.

1.10. Change of fractal dimension in pulmonary vascular disease

Ghorishi et al. reported the mean x_p to be 1.671 at $0.01 \leq r_p \leq 10$ mm in cast-morphometry of a 2-month-old lamb with secondary PH caused by surgically produced L-R shunt in the fetal period [17]. However, x_p in the same shunt lamb targeted 3.0 at the most peripheral pulmonary arterioles ($r_p \leq 0.01$ mm) in their Figure 2B [17], where its x_p stayed around 2.0–2.3 at r_p from 0.4 to 3 mm (Fig. 6).

Most morphometric studies were performed with formalin-fixed specimens or using resin cast method; therefore, their data do not necessarily reflect actual *in vivo* pulsatile hemodynamic realities [3, 66, 76, 80]. Nichols and O'Rourke [66] described the cast technique involves errors that are difficult to allow for [3]. The high injection pressure of resin [17, 20], linear shrinkage [3] of at least 10% on setting [66], the non-physiological temperature of gelatin-barium suspension at 60°C [17, 20], and high viscosity of resin (methylmethacrylate plastic) [3, 17] might not be suitable to estimate the micro-structure at the pulmonary terminal arteriolar level [3, 20].

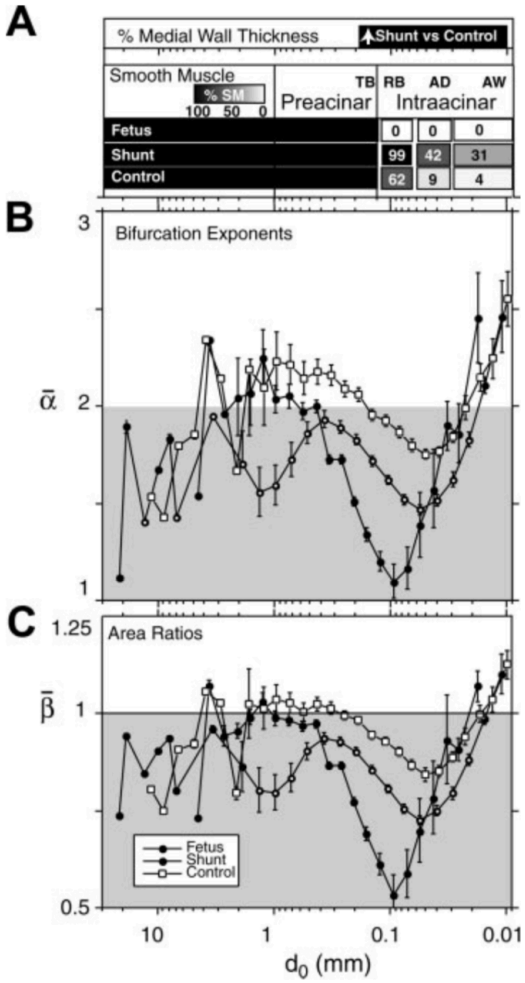

Figure 6. Figure 2 from Ghorishi et al. [17] cited from p. H3009 of *Am J Physiol Heart Circ Physiol* 292: H3006-H3018 (2007) with permission. The figure compares the average value of bifurcation exponents ($\bar{\alpha}$) in the pulmonary arterial tree among fetus, 8-week old control twin, and shunt twin lambs in their resin morphometric study. The aortopulmonary shunt for the shunt twins was created by surgical operation in the uterus 4–8 days before delivery. TB, terminal bronchiole; RB, respiratory bronchioles; AD, alveolar ductus. d_0 stands for diameter; $\bar{\beta}$, the average value of area ratio which compares the sum of the cross-sectional area of the two daughter vessels to that of their mother vessel. Although Ghorishi et al. misapplied black circles for the fetus in the graph legend surrounded by a square, the fetus data should be indicated by white circles.

1.11. The aim of this study

The fractal dimension of the pulmonary arterial tree, which our new method tried to estimate in this analytical study, would supply the vascular architectural information of PVD without histological means. The fractal dimension of the pulmonary arterial tree can be conceivably evaluated by clinical means, such as interpreting classical pulmonary vascular resistance (PVR) on the basis of a fractal network model [12]. PVR, as normalized by the body surface area (*BSA*) in children, has long been used as a simple and convenient parameter to clinically or physiologically evaluate the pathologic state of the pulmonary vascular bed as a whole [22]; however, it has some inevitable drawbacks, such as insufficient capability to locate the exact distribution of peripheral resistance or quantify the actual geographical or structural pathology.

The vascular reaction and its wall remodeling affect diameter, hence tree complexity, which has been shown to influence adaptive changes in the fractal dimension [85, 86] in experimental models of PH [17]. However, whether the fractal dimension changes dynamically in the human condition has not been demonstrated. This model analysis with in vivo hemodynamic data of routine catheterization in voluntary respiration is also important because the actual *in vivo* measurement of hemodynamic data in peripheral pulmonary arteries during voluntary respiration is unfeasible as well as in *in vitro* conditions with artificial positive-pressure ventilation.

Arterial branching is not uniform in a geometric self-similar manner, but it can demonstrate diameter heterogeneity within a resistance partition [12, 17, 66]. In view of the segmentation by Hakim et al. [24, 59, 71], and the possibility of an arterial tree with different dimensions within a given segment, our focus was on the peripheral arterial segment. We developed a fractal model whose dimension x was predicted to reflect vessel radii between 10 and 100 μm. Our hypothesis is that tree complexity changes in conjunction with PH. We evaluated this hypothesis by comparing the pulmonary and systemic model-

derived values.

Such changes, if significant, may indicate a multifractal paradigm of fractal adaptation [19, 56, 94], where dimensions change in response to hemodynamic forces, which is currently not accounted for in Murray's theory alone [3, 19, 41, 48, 55, 82, 88, 93, 94]. Previous studies tried to account for the multifractility of arterial trees in the living body by using multiple optimal conditions corresponding to each fractality [3, 19, 41, 48, 55, 83, 88, 93, 94] because they could not explain the structures using an integrated theory alone. Finally, we discussed two possible theories, i.e. the maximal blood flow hypothesis and the least energy principle, to explain the change in fractal dimension or the multifractility of arterial systems. We hope that our new methodology and theories might contribute to the development of artificial vascular trees and circuits with an optimal design as well as a deep understanding of the vascular pathophysiology including the mechanism of PVD.

2. Methods

2.1. Physiological and pathophysiological premises

For the systemic model we assumed that the mean pressure gradient of large arteries to peripheral arteries $\Delta P_{prox\text{-}s}$ ($r > 100$ μm) : $\Delta P_{peri\text{-}s}$ ($r \leq 100$ μm) was 1:6 (Fig. 7B) as mentioned in the *section 1.1*. The border of radius was defined as 100 μm [66] in this model for simplicity.

Using the analogy of systemic counterparts [66] and on the basis of pressure data directly measured in the isolated perfused dog lung reported by Bhattacharya et al. [6] we applied same 1:6 ratio rule for the mean pressure gradient distribution in the pulmonary circulation between $\Delta P_{prox\text{-}P}$ ($r > 100$ μm) and $\Delta P_{peri\text{-}P}$ ($r \leq 100$ μm), as shown in Figure 7A.

Based upon the canine experimental report by Michel et al., in which they examined the effects of chronic L-R shunt surgically produced between the left subclanian and left lower lobe arteries [59], we assumed tentatively to regard $\Delta P_{cv\text{-}p}$ in PH caused by congenital L-R shunt as remaining stable at the 50% level of the normal trans-pulmonary pressure drop for simplicity irrespective of the underlying PH level (Fig. 7A).

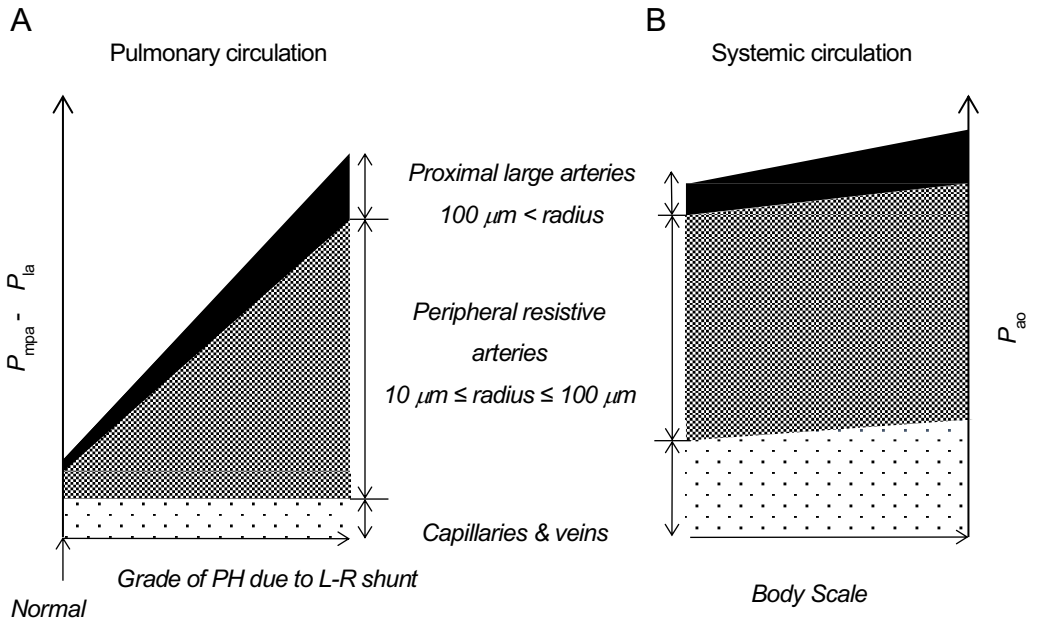

Figure 7. These schemas illustrate the relative longitudinal distribution of three segmental pressure gradients in pulmonary (**A**) or systemic (**B**) circulation in relation to pulmonary hypertension (PH) and systemic blood pressure, respectively. P_{mpa}, P_{la}, and P_{ao} indicate mean pressures in the main pulmonary artery, left atrium, and aorta, respectively. These three segments are proximal large arteries of radius > 100 μm, peripheral resistive arteries of radius 10–100 μm, and capillaries and veins. We applied 1:6 as the ratio between pressure drops through the proximal arteries and through the peripheral arteries [66]. The pressure drop through pulmonary capillaries and veins does not change even in PH due to chronic L-R shunt [59]. Cited from ref. [64].

2.2 Fractal model to translate the q-r relationship of a single vessel into that of the whole vascular tree

The mathematical model in this study was designed with fractal theory and Eq. (10) by translating the relationship between q and r of a single vessel into that between total blood flow (Q) and whole peripheral arterial resistance (R_{peri}) in an arterial network. This model can be applied to the fractal analysis of resistive arteries and peripheral arterial system with hemodynamic data clinically accessible in a routine cath study.

First, we constrained the mean radius of the initial starting 1st resistive arteries as $r_1 = 100$ μm. We expressed the total number of unit arterial trees as scattered in parallel by N_1, which is a natural number (Fig. 8A). Parallel N_1 unit resistive arterial trees were connected to large arteries in-series (Fig. 8A).

Second, we defined the unit resistive arterial tree as an asymmetric branching fractal trees that yield generations from the most proximal 1st to the most peripheral n-th in series, where n is a natural number (Fig. 8B). Setting k as an integer $1 \leq k \leq n$, when the k-th generation vessels whose means of radius, vessel length, and number of vessels are given as r_k, l_k, and N_k, respectively.

Third, applying the data from related literature [12, 35, 36, 53, 75] mentioned in *section 1.3.*, we regarded the mean outlet radius of precapillary arterioles as 10 μm in both systemic and pulmonary vascular trees for simplicity (Fig. 9). We constrained the mean radius of the last n-th arterioles as $r_n = 10$ μm, where N_n terminal arterioles are connected to capillaries (Figs. 8B and 9). Hence, in pulmonary circulation, the resistive arterial network is composed of the intra-acinar arteries [30].

Therefore, this fractal structure neither includes large central arteries, which act more as a Windkessel or an elastic reservoir proximally [59, 66], nor the capillary network, which is not a simple tree but instead a complex sinusoid [87].

We also assumed that practically all resistive arteriolar vessels have the shape of a relatively rigid

circular cylinder in both systemic and pulmonary arterial systems [7, 12, 15, 17, 39, 41, 45, 48, 57, 66, 75, 80, 82, 86, 94].

In addition, we assumed that each repetitively branching arterial tree within the unit network is made of a fractal dichotomy as a whole, as indicated in Figure 8B. Blood flow was treated as a viscous incompressible non-Newtonian fluid [13, 26, 39, 66].

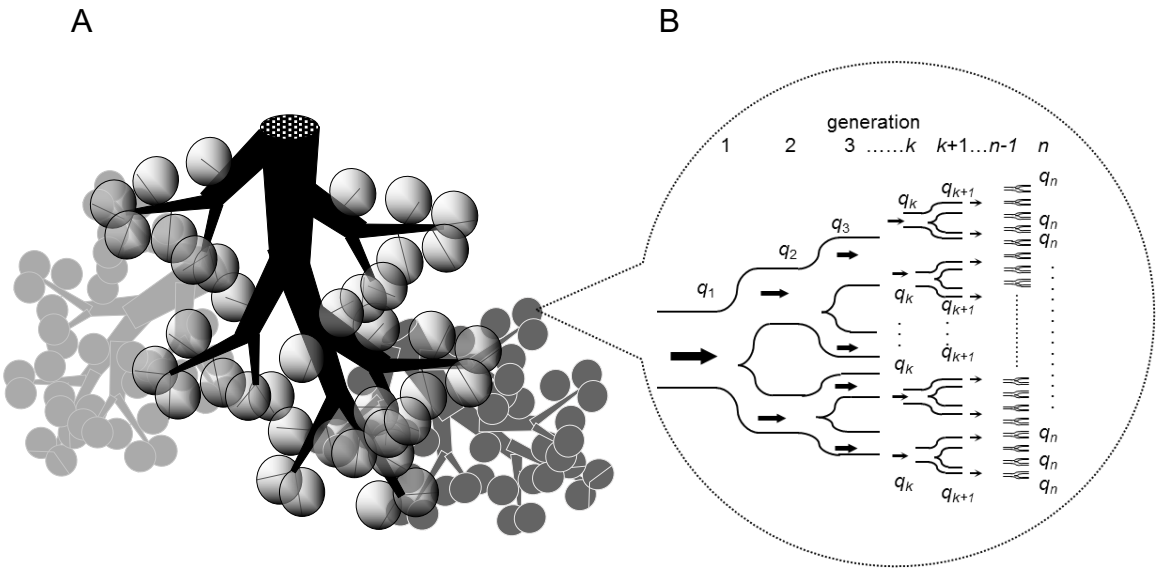

Figure 8. A. Schematic diagram of either the pulmonary or systemic arterial tree. Unit resistive arterial trees, scatted and connected in parallel to the central compliant artery, are represented by circles with a single slender line inside. **B.** Schematic diagram of a unit peripheral resistive arterial tree with the condition of $N = 2$ in Eq. (11a), which starts from the 1st generation, bifurcating repeatedly in series until the terminal n-th. The last n-th generation vessels are distally connected to capillaries. q_k, mean blood flow through k-th generation vessels, where arrows (→) indicate the direction of blood flow; k, natural number from 1 to n. This figure was cited from ref. [64].

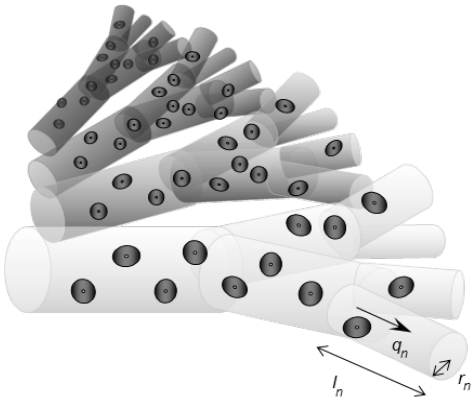

Figure 9. Schematic diagram suggesting the landscape around terminal arterioles. Scattered ovals represent red blood cells (RBCs). The mean radius (r_n) of terminal arterioles is considered to be determined by the scale of RBCs. So, r_n was in common among different species of mammals [12, 35, 36, 53, 74], because the size of mammalian RBCs stays almost same among them. q_n and l_n represent mean blood flow and vessel length of terminal arterioles, respectively. This model set r_n at 10 μm. This figure was cited from ref. [64].

2.2.1. Incorporating this branching fractal structure into the resistive arterial tree

Letting the vessel number, mean radius [μm] and mean length [mm] of the k-th generation (k was a natural number: $1 \leq k \leq n$) be N_k, r_k, and l_k, respectively, we assumed that the fractal structure is ruled by:

$$N = N_{k+1}/N_k, \tag{11a}$$

$$\beta = r_{k+1}/r_k, \tag{11b}$$

$$\gamma = l_{k+1}/l_k, \tag{11c}$$

where N was set at 2 in our model formulation for simplicity because the arterial branching pattern has long been treated as a bifurcation in model analysis of systemic and pulmonary vascular trees [15, 36, 41, 57, 61, 66], although the branching ratio N reported by morphometric studies in the pulmonary arterial tree varied from 1.79 in 2-month-old lamb [17] to 3.58 in cat [91]; $\beta (0 < \beta < 1)$ and $\gamma (0 < \gamma < 1)$ are also assumed to be constants throughout the successive branching generations within a unit peripheral resistive arterial tree and throughout the parallel arranged unit arterial trees. r_k and r_{k+1}, or l_k and l_{k+1} represent the mean values of all vascular radii or lengths of in-series placed individual generations within the unit vascular network. For simplicity, we did not take into consideration in our model the effects of tapering or turbulence within the vessel.

By combining Eqs. (1), (8), (9), (10), (11a), (11b), and (11c), we tried to translate the relationship between the blood flow of a single vessel and its radius to that between the total blood flow and its overall arterial resistance in the whole peripheral vascular network, either pulmonary or systemic.

Hagen–Poiseuille's law and our fractal hypothesis gave us the whole peripheral vascular resistance (R_{peri} [mmHg/L/min]) as:

$$R_{\text{peri}} = \sum_{k=1}^{n} \frac{8\lambda\mu l_k}{N_k \cdot \pi r_k^4}, \ \lambda = \frac{1\times10^{15}}{133\times60} \ [\text{mmHg·min·μm}^4/(\text{L·cP·mm})]. \tag{12}$$

cP (centipoise) is a fluid viscosity unit. λ converts the resistance of the cgs unit into mmHg·min/L.

Because apparent blood viscosity was reported to decrease significantly in vessels with radii < 100 μm using the Fåhraeus–Lindqvist effect which is well known as a non-Newtonian effect of blood flow in the organ regional circulation [13, 26, 39, 66], in this analysis we used the Haynes' equation [26], shown below, letting μ be $\mu(r)$; r, vessel radius:

$$\mu(r) = \frac{\mu_\infty}{(1+r_t/r)^2}, r_t < r. \quad (13)$$

Here μ_∞ and r_t are estimated as 4.0 cP and 4.29 μm, respectively (Fig. 10) [13, 26, 39, 66].

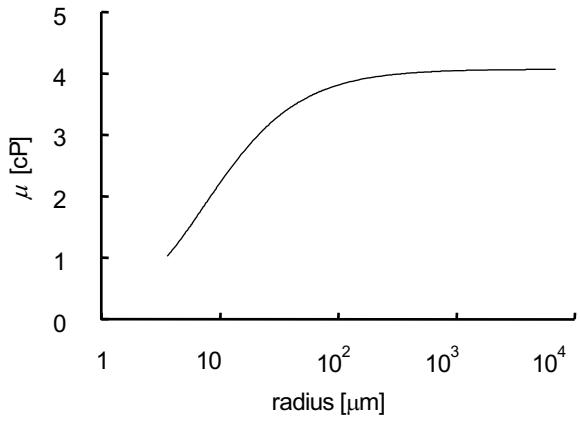

Figure 10. The simulation curve of Fåhraeus–Lindqvist effect [13, 26, 39, 66] reported as Haynes' equation [26, 39]. μ represents the blood viscosity given as centipoise (cP); r, radius. Figure 10 was cited from ref. [64].

When we introduced a constant for the relative radius ratio $\delta = r_t / r_n$ into our computation tentatively and for convenience, δ in the next Eq. (14b) became 0.429 (= 4.29/10). Rewriting Eq. (12) with Eqs. (11a), (11b), (11c), (13), and δ yields:

$$R_{\mathrm{peri}} = \sum_{k=1}^{n} \frac{8\lambda\mu_\infty l_k}{N_k \cdot \pi r_k^4 (1 + r_t/r_k)^2} = \frac{8\lambda\mu_\infty l_n}{\pi N_1 r_n^4} \cdot G(n), \tag{14a}$$

where

$$G(n) = \sum_{k=1}^{n} \frac{\gamma^{-(n-k)}}{N^{k-1} \cdot \beta^{-4(n-k)} \left(1 + \delta\beta^{n-k}\right)^2}. \tag{14b}$$

$G(n)$ is a tentatively introduced intermediary function as derived from the fractal structure in order to combine and translate n, N, β, and γ into R_{peri}.

Letting the mean blood flow [L/min] in each n-th generation vessel and blood flow of total arterial network be q_n and Q, respectively (Fig. 8B), Eq. (10) gives:

$$q_n = \varepsilon \cdot r_n^x = Q / N_n. \tag{15}$$

By using Eq. (15), elimination of r_n from Eq. (14a) yields:

$$R_{\mathrm{peri}} = Q^{-4/x} \cdot (\varepsilon \cdot N_n)^{4/x} \cdot \frac{8\lambda\mu_\infty l_n}{\pi N_1} \cdot G(n). \tag{16}$$

Although the vessel length l_n [mm] can be regarded as an invariable for blood flow change [66], we designed the vessel length to be proportional to a body scale parameter, M, for standardization. The way to define the most proper M is described in the Results section.

So, letting d_n be the proportional coefficient, l_n is given by:

$$l_n = d_n \cdot M. \tag{17}$$

Eqs. (14a), (15), (16), and (17) result in an important logarithmic equation to define Q as a function of R_{peri}:

$$\ln Q = A \cdot \ln\left(\frac{R_{\mathrm{peri}}}{M}\right) + B, \tag{18}$$

where

$$A = -\frac{x}{4}, \tag{19a}$$

$$B = \ln\left\{\varepsilon N_n \left(\frac{8\lambda\mu_\infty d_n G(n)}{\pi N_1}\right)^{x/4}\right\}. \tag{19b}$$

Thus, Eq. (18) defines the final relationship among Q, R_{peri}, and M in the whole vascular bed, either

pulmonary or systemic. Furthermore, Eqs. (18) and (19a) provide us with a method to analytically estimate the key parameter, namely the *radius exponent x* [55], even from routine *in vivo* hemodynamic catheterization data.

A, *B*, and *x* of both vascular beds were then determined for each categorized group of patients (Table 1) along with *x*-derived *n*, β, and γ. We also analytically quantified N_1, the number of unit peripheral resistive arterial trees counted at the inlet, and N_w, the whole number of arteries included in all the vascular networks in question where the peripheral resistance resides.

2.2.2. Determination of x, A, & B

Setting pulmonary blood flow and peripheral pulmonary arterial resistance as Q_p and $R_{peri\text{-}p}$, respectively, $\ln Q_p$ was plotted against $\ln(R_{peri\text{-}p}/M)$ in a logarithmic scale diagram for each group. Linear regression analysis was performed for each group using the least-square method. The slope corresponds to A_p while its intercept to B_p, respectively. x_p is given by Eq. (19a). A_s, B_s, and x_s were also determined similarly.

2.2.3. Estimation of n, β, γ, N_1, & N_w

Because the total blood flow should be equal to the sum of all the *n*-th generations in this arterial tree (Fig. 8B), Eq. (20) ensues from Eq. (10):

$$Q = N_1 \varepsilon r_1^x = N_1 N^{n-1} \varepsilon r_n^x \approx 2^{n-1} N_1 r_n^x, \tag{20}$$

where *x* and ε eventually represent averaged values for each item for the whole resistive arterial bed. Using the constraints of r_1 = 100 μm and r_n = 10 μm as primary constants in this model, Eq. (20) gives *x*-derived *n* as the mean real number ($\tilde{n}$) in each group:

$$\tilde{n} = x \cdot \frac{\ln(100/10)}{\ln 2} + 1 = \left(\frac{\ln 10}{\ln 2}\right) x + 1 \approx 3.32x + 1. \tag{21}$$

To deal with *n* and calculate *G*(*n*), however, we chose the nearest natural number in place of $\tilde{n}$ as *n*.

As Eq. (11b) results in $r_n = \beta^{n-1} r_1$ from the model structure, Eq. (22) follows using $\tilde{n}$ of Eq. (21) for *n*:

$$\beta = \left(\frac{10}{100}\right)^{\frac{1}{n-1}} = 0.1^{\frac{1}{n-1}} \approx 0.1^{\frac{1}{3.32x}}. \tag{22}$$

Similarly, Eq. (11c) gives $l_n = \gamma^{n-1} \cdot l_1$ by definition. Letting d_1 be the proportional coefficient as in Eq. (17), l_1 can also be represented as a proportion to *M*: $l_1 = d_1 \cdot M$. Using d_1 and d_n, γ can also be obtained as:

$$\gamma = \left(\frac{d_n}{d_1}\right)^{\frac{1}{n-1}} \approx \left(\frac{d_n}{d_1}\right)^{\frac{1}{3.32x}}. \tag{23}$$

Combination of Eqs. (14a), (17), and r_n = 10 μm results in:

$$N_1 = \frac{8\lambda \mu_\infty d_n G(n)}{10^4 \pi (R_{\text{peri}}/M)}. \tag{24}$$

N_w was also computed as:

$$N_w = \sum_{k=1}^{n} N^{k-1} N_1 = \frac{N^n - 1}{N - 1} \cdot N_1 \approx (2^n - 1) \cdot N_1. \tag{25}$$

Thus, N_1 and N_w were calculated for each patient and standardized conventionally by *BSA* [m^2].

2.3 Subjects

2.3.1. Subject data

Cardiac catheterization was performed as one of the preoperative evaluations from November 1996 until June 2007 in the Department of Pediatrics, Tokyo University Hospital. All patients had either a normal or increased ratio of pulmonary (Q_p) over systemic (Q_s) blood flow: $Q_p/Q_s \geq 1$. In 213 patients, the mean pressure of the pulmonary arterial wedge (P_{paw} [mmHg]) was recorded and regarded as that of the left atrium (P_{la} [mmHg]) [9, 11]. These 213 patients had neither a reversed right-to-left (R-L) shunt deriving from pulmonary hypertension (PH) by advanced PVD nor restrictive or obstructive lung diseases. They also had no systemic vascular diseases.

2.3.2. Categorization of the patients with an L-R shunt

As shown in Table 1, we categorized our patients with L-R shunt into seven groups according to the degree of transpulmonary vascular pressure gradient or the mean pressure of main pulmonary artery (P_{mpa} [mmHg]) minus P_{paw}.

Approximately 30% of VSD patients in Japan and other Far Eastern countries [80] have a so-called outlet (or subaortic) defect or type I by Kirklin [43] where the right coronary cusp often prolapses down into the left ventricle and obliterates the defect from birth with the result of only a trivial shunt across the defect even if the defect is not small, whereas its incidence is reported to be approximately 5–7% in America or European countries [2, 77, 81]. These patients are consequently categorized into controls because they show only a tiny shunt across the defect at the time of cardiac catheterization, even though their original defect was not small and early surgical intervention is imperative because prolapsed cusp eventually induces significant aortic regurgitation and timely surgery prevents this untoward complication.

Most of our VSD control patients belonged to this type of tiny shunt subaortic defect. The only ASD patient had a tiny defect and 2 PDA patients had such a rudimentary ductus that it was barely visualized by angiography. We termed patients with type I VSD with right coronary cusp prolapse but without aortic regurgitation, 2 small PDAs without indication for coil embolization, and a small ASD, controls because they were quite healthy without any physical disability or stunted growth by the disease ($Q_p/Q_s \approx 1.0$).

Table 1. Categorization, number of patients, and distribution of shunt site for each group.

Group	Indices of categorization		Number of patients	Number of patients for each shunt site		
	$P_{mpa} - P_{paw}$ [mmHg]	Q_P/Q_S		A	V	D
Control	≤ 9	1.0	19	1	17	2
1	≤ 9	> 1.0	47	6	38	4
2	≥ 10 – ≤ 15	> 1.0	53	10	41	4
3	> 15 – ≤ 25	> 1.0	29	8	23	5
4	> 25 – ≤ 35	> 1.0	20	4	16	7
5	> 35 – ≤ 45	> 1.0	22	4	21	2
6	> 45	> 1.0	23	3	19	4

P_{mpa}, mean pressure in the main pulmonary artery; P_{paw}, mean pressure in the pulmonary arterial wedge; Q_P/Q_S, pulmonary to systemic blood flow ratio; A, atrial; V, ventricular; D, ductal. Note that a single patient might have more than one left-to-right shunt. Table 1 was cited from ref. [63].

2.3.3. Estimation of the reversibility in the severe pulmonary hypertension.

To determine whether PH due to L-R shunt is irreversible a 100% oxygen administration test was additionally performed for patients with severe PH, Gr. 5 or 6, as a preoperative evaluation of vasoreactivity at the time of catheterization [28]. All patients in this study passed the test and showed enough vasoreactivity to be good candidates for surgery. Furthermore, postoperative PH returned to normal even in patients with Gr. 5 or 6 at least within several weeks at most after corrective surgery as assessed by postoperative direct monitoring or echocardiography [10], suggesting that they did not have irreversible PVD in peripheral resistive arteries. Gr. 5 and/or 6, therefore, does not indicate a morphologically advanced stage of PVD.

2.3.4. Cardiac catheterization and estimation of hemodynamics.

Cardiac catheterization was performed by the conventional method [22]. Each patient was sedated by intravenous injection of pentazocine (0.5–1.0 mg/kg) and midazolam (0.2–0.3 mg/kg) to a physiological steady state with voluntary respiration in room air [63]. We evaluated Q_p and Q_s by Fick's method with estimated oxygen consumption, which was assessed by the regression equation fitted by gender, body weight, body length, and heart rate, as was recently reported by Lundell BP et al. [54]. $R_{peri\text{-}p}$ was obtained by:

$$\Delta R_{\mathrm{peri}} = \frac{\Delta P_{\mathrm{peri}}}{Q_{\mathrm{p}}}, \tag{26}$$

where $\Delta P_{peri\text{-}p}$ was estimated as:

$$\Delta P_{\mathrm{peri-p}} = \frac{6}{7}\left(P_{\mathrm{mpa}} - P_{\mathrm{paw}} - \Delta P_{\mathrm{cv-p}}\right) \tag{27}$$

in this analysis as described at the beginning of the Methods. If we regard the $\Delta P_{cv\text{-}p}$ of controls as a half of transpulmonary pressure gradient [6, 7, 24, 59, 63, 71]:

$$\Delta P_{\mathrm{cv-p}} = \frac{1}{2}\left(P_{\mathrm{mpa}} - P_{\mathrm{paw}}\right), \tag{28}$$

the mean and standard deviation (SD) of $\Delta P_{cv\text{-}p}$ in controls is 3.3 ± 0.6 mmHg [63]; therefore, we assumed that $\Delta P_{cv\text{-}p}$ for Gr. 1–6 remained constant at 3.3 mmHg [59, 63].

We calculated $\Delta P_{peri\text{-}s}$ and $R_{peri\text{-}s}$ respectively using [66]:

$$\Delta P_{\mathrm{peri-s}} = 0.6 \times P_{\mathrm{ao}}$$

and $$R_{\mathrm{peri-s}} = 0.6 \times \frac{P_{\mathrm{ao}}}{Q_{\mathrm{s}}}.$$

The general characteristics and hemodynamic data obtained for each group are shown in Tables 2 and 3, respectively.

Table 2. General characteristics of each group.

Group	Age [months]	Gender [M/F]	*BW* [kg]	Ht [%]
Control	50 (3–195)	8/11	15.7 (5.4–66.6)	38. 7 ± 3.7
1	27 (1–361)	24/23	11.7 (4.0–57.8)	38.3 ± 2.9
2	19 (2–401)	25/28	10.6 (3.8–55.2)	38.5 ± 2.8
3	10 (3–132)	13/16	7.2 (3.9–50.5)	37.8 ± 3.6
4	7 (1–115)	12/8	5.5 (3.0–14.0)	36.5 ± 2.8
5	5 (2–152)	10/12	5.2 (2.0–47.9)	37.6 ± 3.5
6	4 (2–102)	14/9	5.6 (3.7–20.3)	37.7 ± 3.8

M, male; F, female; *BW*, body weight; Ht, hematocrit. Age & *BW* are represented as the median with (range); Ht, mean ± SD. Student's t-test found no significant differences among these 7 groups with respect to gender ratio or Ht. Note that patients with severe pulmonary hypertension with a bigger defect had a greater opportunity for earlier hemodynamic study (catheter) and earlier surgical intervention to protect against advanced or irreversible pulmonary vascular disease. Table 2 was cited from ref. [63].

Table 3. Hemodynamic data of each group.

Group	Q_p/BSA [L/(min·m^2)]	$R_{peri\text{-}p}\cdot BSA$ [mmHg·min·m^2/L]	Q_s/BSA [L/(min·m^2)]	$R_{peri\text{-}s}\cdot BSA$ [mmHg·min·m^2/L]
Control	6.1 ± 1.3	0.5 ± 0.1	6.1 ± 1.3	7.9 ± 1.5
1	7.1 ± 2.8	0.6 ± 0.2	5.0 ± 1.4	9.3 ± 2.7
2	7.5 ± 2.7	1.2 ± 0.5	5.0 ± 1.6	9.4 ± 2.5
3	8.1 ± 2.9	1.8 ± 0.6	4.4 ± 1.4	10.2 ±2.7
4	8.3 ± 3.0	3.2 ± 1.3	4.2 ± 1.1	10.4 ± 2.2
5	7.9 ± 2.9	4.4 ± 1.4	3.9 ± 0.7	10.3 ± 1.5
6	7.0 ± 2.8	6.8 ± 3.2	3.8 ± 1.1	12.3 ± 5.2

Q_p and Q_s stand for pulmonary and systemic blood flow; $R_{peri\text{-}p}$ and $R_{peri\text{-}s}$, estimated pulmonary and systemic peripheral arterial resistance, respectively; *BSA*, body surface area. Data are represented as the mean ± SD. Note that these $R_{peri\text{-}p}$ and $R_{peri\text{-}s}$ are estimated as 40–80% and 60% of ordinary pulmonary and systemic vascular resistance used clinically and conventionally. Table 3 was cited from ref. [63].

2.4. Ethical procedures

This study was permitted to use the clinical data from patients by the directors of the Department of Pediatrics (T. I.) and Pediatric Cardiology (H. K.), in accordance with guidelines of the time of the study: *Comprehensive Retrospective Studies of the Epidemiology, Pathophysiology, Diagnosis, and Therapeutics of Pediatric Diseases in the Department of Pediatrics of the University of Tokyo Hospital*.

3. Results

3.1. Systemic circulation and the importance of body length in the new model

The relationship between systemic blood flow (Q_s) and peripheral systemic arterial resistance ($R_{peri\text{-}s}$) was analyzed. First the simple plot of lnQ_s vs. ln $R_{peri\text{-}s}$ of all patients is presented in Figure 11A. lnQ_s and ln $R_{peri\text{-}s}$ turned out to be linearly arranged. As conventionally standardized by *BSA* ln(Q_s/*BSA*) vs. ln($R_{peri\text{-}s}$·*BSA*) are presented in Figure 11B for reference.

Then, three different body scale parameters for *M* were introduced to standardize R_s as indicated in Eq. (18). We compared the regression slope and correlation coefficient for each *M*, e.g. *BSA*, body weight (*BW*), and body length (*BL*) as shown in Figures 11C, 11D, and 12, respectively. *BL* was defined as the distance from the top to heel.

When *BSA* and *BW* were applied to Eq. (18) as *M*, the slope (= A_s) of the regression line resulted in -0.637 (Fig. 11C) and -0.549 (Fig. 11D), respectively, with close negative correlations (r = -0.985 and -0.981, respectively). Finally, the plot applying *BL* to Eq. (18) was presented in Figure 12. lnQ_s vs. ln($R_{peri\text{-}s}$/*BL*) plots exhibited A_S = -0.721 (r = - 0.983) in controls (Fig. 12A), and A_s = -0.776 (r = 0.987) in all patients under study, respectively (Fig. 12B).

The regression line with the least scatter was found in Figure 12B, where *BL* was used as the most suitable body scale parameter. Furthermore, with Eq. (18) these values of *A* resulted in $x = 2.9–3.1$, which fluently accounted for Murray's law. On the other hand, *BSA* and *BW* did not represent Murray's law from their regression slopes with a result of $x = 2.5$ and $x = 2.2$, respectively.

Therefore, introduction of *BL* is appropriate to adjust for different vessel lengths and meet Murray's law in systemic resistive arteries. Thus, *M* in Eq. (18) was rewritten with *BL* and completed as:

$$\ln Q = A \cdot \ln\left(\frac{R_{\mathrm{peri}}}{BL}\right) + B. \tag{29}$$

We attempted to apply Eq. (29) to pulmonary circulation similarly.

A_s, x_s, and B_s stayed almost constant throughout all groups (Figs. 14A and B). Mean ± SD for A_s was -0.77 ± 0.04, for x_s 3.1 ± 0.2, and for B_s 3.25 ± 0.11. Calculated $\tilde{n}_s$ by Eq. (21) was 11.3 ± 0.5 (Table 4). Meanwhile, $l_{1\text{-}s}$, $l_{n\text{-}s}$, $d_{1\text{-}s}$, and $d_{n\text{-}s}$ in Eq. (23) were worked out as follows. First, we assumed that $l_{1\text{-}s}$ = 4.0 mm and $l_{n\text{-}s}$ = 0.65 mm from microscopic measurements of a dog weighing 20 kg [61] because no human data of systemic vessel length were available. A 20-kg body weight corresponds to BL = 1.14 min humans [47], we assumed $d_{1\text{-}s}$ = 3.51 (= 4.0/1.14) and $d_{n\text{-}s}$ = 0.57 (= 0.65/1.14) to be the equivalent human systemic measurements and the best possible substitution. Therefore, by applying these data and our result for x_s to Eqs. (22) and (23), β_s and γ_s in systemic arteries were 0.80 ± 0.01 and 0.84 ± 0.01 (Table 4 and Fig. 15). Results of $N_{1\text{-}s}$ and $N_{w\text{-}s}$ are presented in Figure 16, in which they were standardized with BSA.

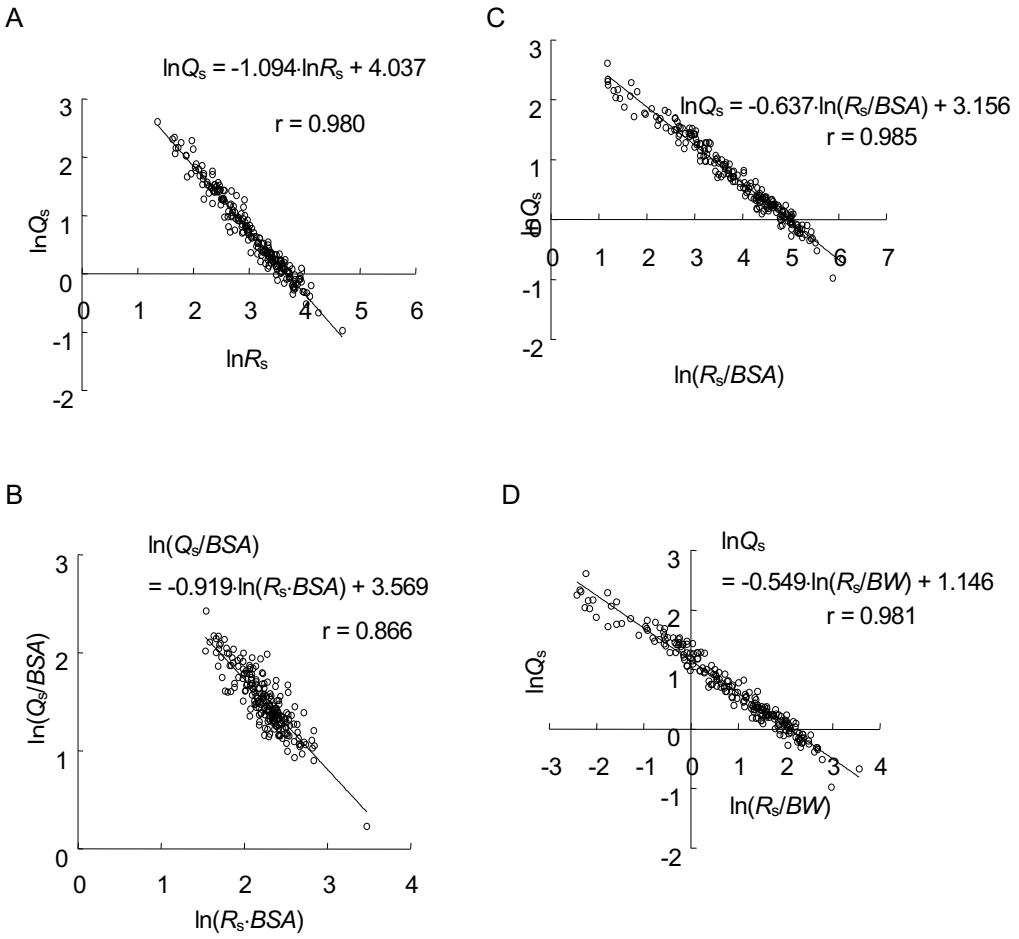

Figure 11. A. Simple plot of lnQ_s vs. lnR_s. **B.** Plot of ln(Q_s/*BSA*) vs. lnR_s·*BSA*. **C.** Plot of lnQ_s vs. ln(R_s/*BSA*). **D.** Plot of lnQ_s vs. ln(R_s/*BW*). Q_s, R_s, *BSA*, and *BW* stand for systemic blood flow [L/min], peripheral systemic arterial resistance [mmHg/L/min], body surface area [m^2], and body weight [kg]. The regression line was fitted by the least square method. r stands for correlation coefficient. Figures were cited from ref. [64].

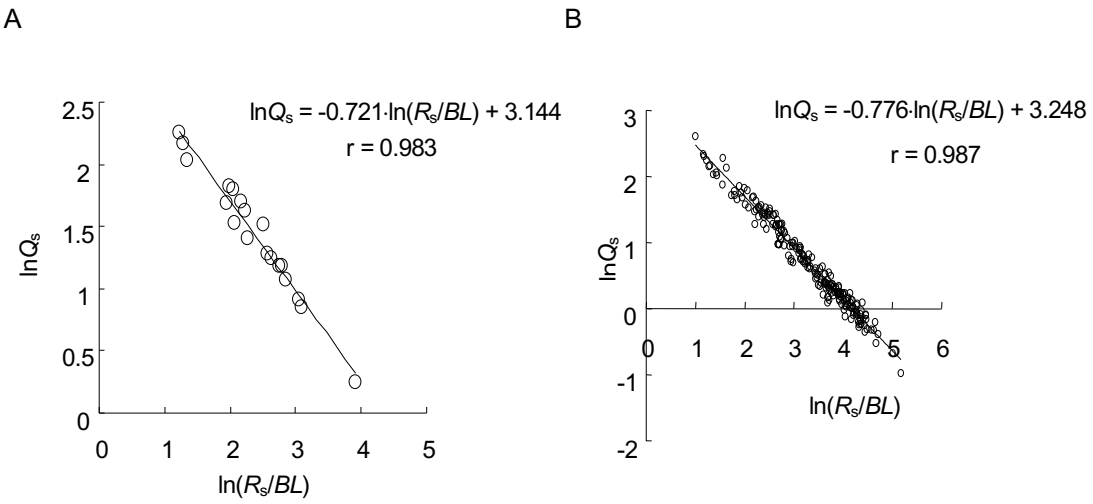

Figure 12. lnQ_s vs. ln(R_s/BL). **A.** Plot of controls. **B.** Plot of all patients. Q_s, R_s, and BL stand for systemic blood flow [L/min], peripheral systemic arterial resistance [mmHg/L/min], and body length [m], respectively. The regression line was fitted by the least square method. r stands for correlation coefficient. Figures were cited from ref. [64].

3.2. Application of this model to normal pulmonary circulation

Figure 13A presents the plot of $\ln Q_p$ vs. $\ln R_{peri\text{-}p}/BL$ in our control group. The regression slope A_p yielded $x_p = 2.2$ (Fig. 14A). Calculated $\tilde{n}_p$ by Eq. (21) was 8.3 in controls (Table 4).

Because $l_{1\text{-}p}$ and $l_{n\text{-}p}$ have been reported to be 1.08 ± 0.65 and 0.22 ± 0.08 mm in the pulmonary cast study of adult human males with $BL = 1.83 \pm 0.03$ m [47], we assumed both $d_{1\text{-}p}$ and $d_{n\text{-}p}$ in Eq. (23) were 0.59 (= 1.08/1.83) and 0.12 (= 0.22/1.83), respectively. As a result, β_p and γ_p in normal pulmonary circulation were estimated as 0.73 and 0.80, respectively (Table 4 and Fig. 15).

3.3. Application to the pulmonary circulation with L-R shunt

$\ln Q_p$ vs. $\ln(R_{peri\text{-}p}/BL)$ plots of all groups are shown in Figure 13B. The least-square fittings and the resultant linear regression equations were in good agreement with Eq. (29) and the correlation coefficient (r) of each group of the peripheral pulmonary arterial bed as well as the systemic one ranged from -0.95 to -0.99, indicating that flow in these patients was strictly governed by the resistance of the whole peripheral arterial bed as divided by BL again.

Figure 13B shows the gradually decreasing slope of regression lines in relation to the severity of PH. The changes in slope resulted in the increment of x_p from 2.2 to 3.0 (Fig. 14A). Changes in estimated β_p and γ_p in terms of the severity of PH are presented in Table 4 and Figure 15. B_P had a high correlation with $\ln \Delta P_{peri\text{-}p}$, as presented in Figure 14B. Intercept B means $\ln Q$ expected theoretically in condition of $R/BL = 1$ by Eq. (29).

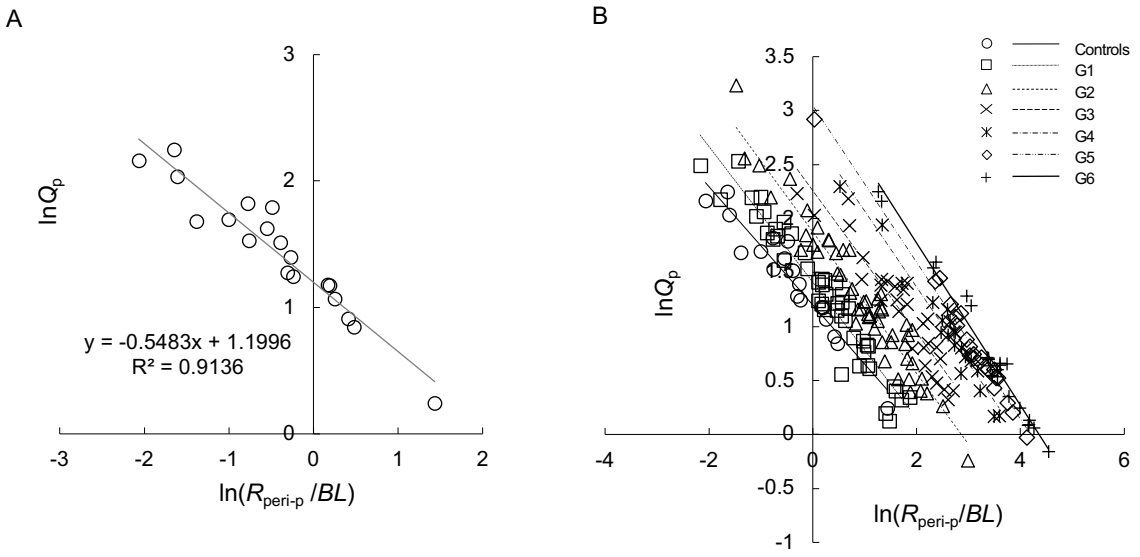

Figure 13. lnQ_p vs. ln(R_p/BL). **A.** Plot of controls. **B.** Plot of all subjects categorized into 7 groups including controls in terms of severity of pulmonary hypertension induced by left-to-right shunt. Q_p, R_p, and BL stand for pulmonary blood flow [L/min], peripheral pulmonary arterial resistance [mmHg/L/min], and body length [m], respectively. P_{mpa} and P_{la} indicate mean pressures of the main pulmonary artery and left atrium, respectively. Q_p/Q_s stands for the ratio of pulmonary vs. systemic blood flows; r, the correlation coefficient. The regression line was fitted to the least. Figures were cited from ref. [63, 64].

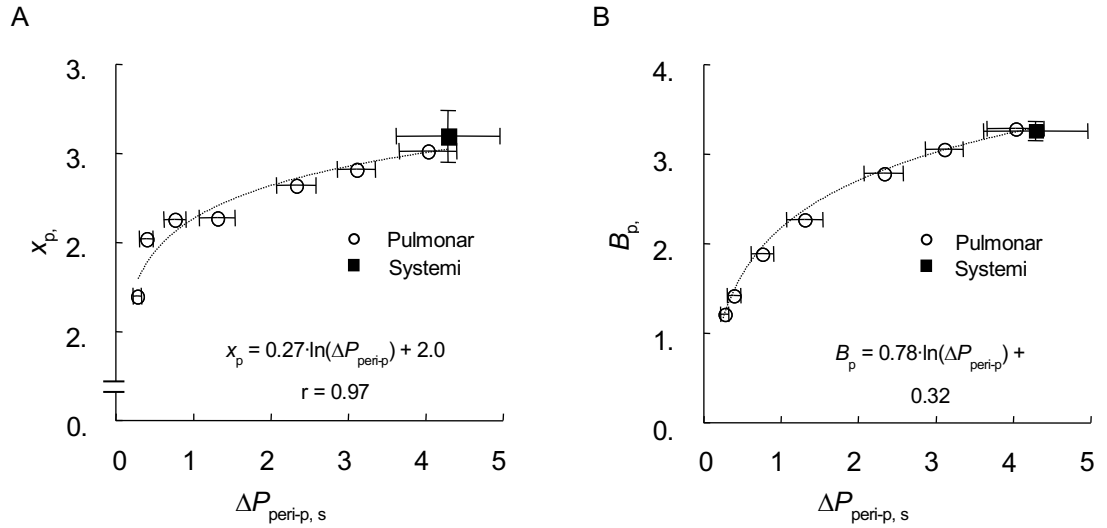

Figure 14. A. The change of x_p with peripheral pressure gradient ($\Delta P_{peri\text{-}p}$). **B.** The increase of B_p with $\Delta P_{peri\text{-}p}$. x is given by Eq. (19a) from the regression coefficient in Figures 12 and 13, and B is the regression constant. Suffixes p and s stand for pulmonary and systemic, respectively. Dashed curves represent the change in x_p or B_p to $\Delta P_{peri\text{-}p}$ by fitting a logarithmic function with the least-square method; r, correlation coefficient. Mean $\Delta P_{peri\text{-}p}$ of each group and mean $\Delta P_{peri\text{-}s}$ of all cases are indicated horizontally with standard deviation (SD) using outliers. Means of x_s and B_s in all groups are similarly presented with SD. Figures were cited from ref. [63].

Table 4. Parameters for fractal structure and the resistance of a partial arterial tree distal to the 8th order estimated using our model.

Group	$\tilde{n}$	β	γ	R_{8th} ($\times 10^5$ [mmHg·min/L])
Pulmonary				
Control	8.3	0.73	0.80	2.9
1	9.4	0.76	0.84	3.8
2	9.7	0.77	0.84	4.3
3	9.7	0.77	0.84	4.4
4	10.4	0.78	0.85	5.2
5	10.7	0.79	0.85	5.6
6	11.0	0.79	0.85	6.2
Systemic	11.3 ± 0.5	0.80 ± 0.01	0.84 ± 0.01	33.8 ± 4.0

R_{8th}, resistance of a partial arterial tree distal to the 8th order for BL = 1.2 [m]. Systemic data are presented as mean ± SD for all groups. Table 4 was cited from ref. [63].

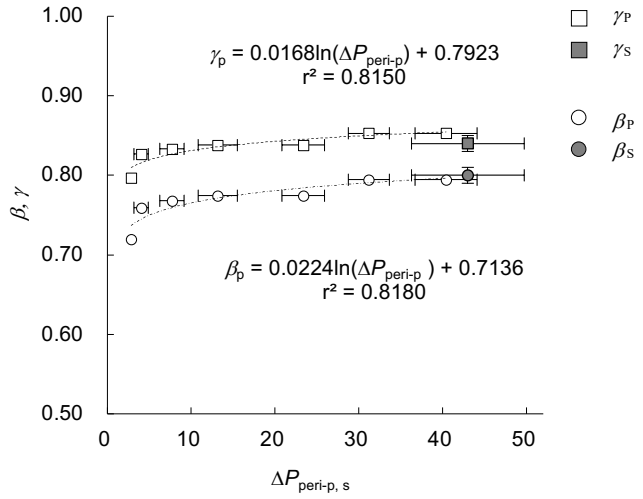

Figure 15. Those of β and γ in relation of ΔP_{peri}. Mean with ± one standard deviation is presented as the circle with horizontal outliers. Dashed curves represent the change in x_p, β_p, or γ_p to ΔP_p by fitting a logarithmic function with the least-square method. r represents the correlation coefficient. ΔP means the peripheral arterial pressure drop; suffix P, pulmonary. Systemic ΔP is estimated as 60% of mean aortic pressure (*section 2.3.4*), whereas pulmonary one as six-sevenths of a half of transpulmonary pressure gradient (Eqs. (27) and (28)), which is given by mean pulmonary arterial pressure minus mean left arterial one. Figure 15 was cited from ref. [64] after modification.

In Figure 16 $N_{1\text{-p}}/BSA$ and $N_{\text{w-p}}/BSA$ showed markedly strong negative correlations with $\ln P_{\text{mpa}}$ (r = -0.88, -0.78, respectively), whereas their systemic counterparts $N_{1\text{-s}}/BSA$ and $N_{\text{w-s}}/BSA$ showed much weaker correlations (r = -0.40 for both). $N_{1\text{-p}}/BSA$ of Gr. 5 and 6 were estimated as 1/43 and 1/55 of the controls, whereas $N_{\text{w-p}}$/BSA in either Gr. 5 or 6 was only but still approximately 1/9 of the controls. $N_{1\text{-s}}/BSA$ and $N_{\text{w-s}}/BSA$ showed the same negative correlation coefficient against $\ln P_{\text{mpa}}$ because $N_{\text{w-s}}$ is given by $(2^{11.3} - 1)\cdot N_{1\text{-s}}$.

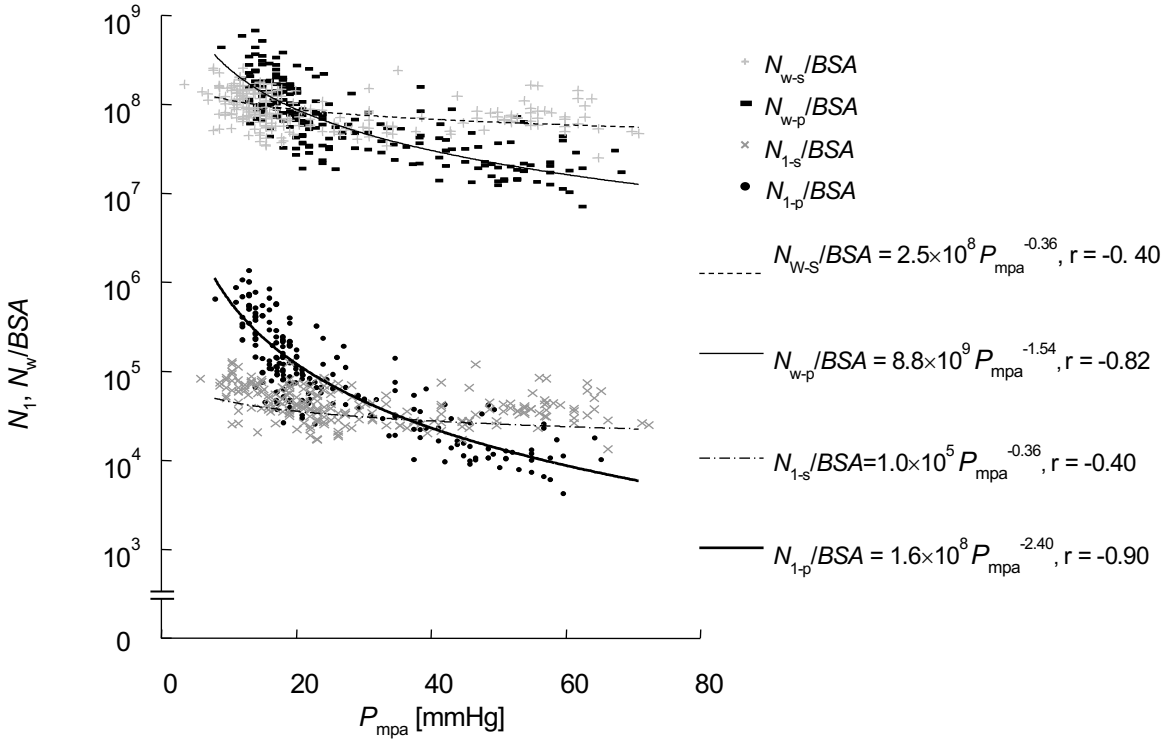

Figure 16. Plot of $N_{1\text{-p}}/BSA$, $N_{1\text{-s}}/BSA$, $N_{\text{w-p}}/BSA$, and $N_{\text{w-s}}/BSA$ vs. P_{mpa}. N_1, number of unit peripheral arterial trees estimated by Eq. (24); N_{w}, whole number of peripheral resistive arteries given by Eq. (25); P_{mpa}, mean pressure of main pulmonary artery [mmHg]. Suffixes p and s represent pulmonary and systemic, respectively. *BSA*, body surface area [m^2]. Lines are exponential regression curves; r, correlation coefficient. Figure 16 was cited from ref. [63].

4. Discussion

A new mathematical simulation model was proposed by combining the fundamental hydrodynamics of a single tube with a morphologically fractal unit network structure, arranged in parallel at the segment of peripheral resistive arteries. The model enabled us to quantitatively transform the basic flow vs. vessel radius relationship of a single tube into that of total flow vs. overall resistance of the peripheral arterial bed where the actual resistance resides in both pulmonary and systemic vessels, and advanced stages of PVD may also develop over time without surgical intervention.

By directly fitting the body scale and in vivo hemodynamic data (BL, Q, R_{peri}) from patients, we successfully determined the key parameters of branching exponents x_p and x_S of our fractal model structure in humans along with some x-derived structural parameters in *in vivo* vasoconstriction by multiple natural neurohumoral feedback mechanisms [37, 59, 69] and down regulation in the number of intra-acinar arteries, which was reported histologically in literatures and caused by unknown mechanism at present [31, 59, 69, 70, 83].

As discussed below, a number of new x-derived parameters depicted the pathophysiological hemodynamics as a reaction to abnormally augmented pulmonary blood flow in terms of its geographic distribution within the arteriolar fractal network.

4.1. Fractal dimension in peripheral systemic arteries

In controls as well as in other groups, x_s stayed almost invariably at 3.1 irrespective of the underlying conditions (Figs. 12 A and B). Resultant x_s in our model was compared with reported counterparts in previous reports [35, 41, 53, 57, 72, 75] and was in good agreement with them (Table 5). That indicated the simultaneous implementation of both functional and structural optimizations, accounted for by the minimum work principle and space-filling embedding, respectively [15, 35, 55, 57, 62].

The importance of *BL* was also recognized in this study as the most proportional coefficient to standardize the vessel length among *BSA*, *BW*, and *BL* itself (Figs. 11 and 12).

Table 5. The radial exponent *x* in the peripheral systemic and pulmonary arteries in previous reports in comparison with our model-derived *x*.

	Radius [μm]	*x*	Method/Data	Reference
Systemic				
Rat, CMA	5*–50	2.73	IM/Fr	[35, 53]
Rat, CMA	3*–54	3.01 ± 0.07	IM/Fr	[57]
Dog, arterioles	11–96	2.947	FA/Mm	[75]
Pig, coronary arteries	4.5*–25	3	FA/Mm	[41]
Human, cerebral arteries	< 500	2.9 ± 0.7	FA/Ag	[72]
Our model, human	10–100	3.1 ± 0.2	MA/Hd	[63]
Pulmonary				
Rat	13–800	2.15	FA/Mm	[38]
Cat	12–508	2.35	FA/Mm	[91, 95]
Human	30*–500	2.3 ± 0.1	FA/Mm	[82]
Our model, human	10–100	2.2	MA/Hd	[63]

* Represents not the mean radii of terminal arterioles but the minimum. CMA indicates cremaster muscle arteries. IM, *in vivo* measurement; FA, fractal analysis; MA, model analysis; Fr, data of flow and radius; Mm, morphometric data; Ag, angiographic data; Hd, hemodynamic data. Data are presented as mean with one standard deviation. Table 5 was cited from ref. [64].

4.2. Fractal dimension in peripheral pulmonary arteries and with L-R shunt

In addition to functional and morphological changes caused by large shunt and PH, x_p increased from 2.2, which was in good agreement with the data as reported by previous morphometric studies [38, 82, 91, 95] (Table 5), to a plateau value of 3.0 according to the grade of PH (Figs. 13A and B).

Ghorishi et al., on the other hand, used resin cast morphometry and reported that the average fractal dimension (equivalent to x in our model) for the whole pulmonary arterial tree in a 2-month-old lamb with an in-utero placed artificial L-R shunt remained at 1.7 (Fig. 6), resulting in two-fold increased bifurcations and retaining its fetal characteristics [17]. Pulmonary arteriolar development was reported to be disturbed and its new morphological pathology manifested itself after 2 months of age in large shunt defects [31, 37, 69, 70]. These lambs were dissected before that age, whereas most patients with Gr. 5 and 6 are already older than 2 months (Table 2).

Furthermore, most samples in their morphometry came from more proximal arteries or even started with main pulmonary artery, extending all the way down to arterioles, as they mentioned in their method [3, 17]. Consequently, their average fractal dimension reflected the situation of more proximal arteries than ours. Because our model deals with more distal resistive intra-acinar arteries theoretically, our radial exponent x_p reflects the estimate of the most peripheral arterioles and their bifurcations, whose number exceeds more than half of whole resistive arterioles because even $N_{n\text{-p}}$ ($= 2^{\tilde{n}-1} \cdot N_{1\text{-p}}$) alone amounts to one half of $N_{w\text{-p}}$ ($= (2^{\tilde{n}} - 1) \cdot N_{1\text{-p}}$), as indicated by the model structure and Eq. (25).

4.3. Fractal parameters

Taking N, which does not influence x as exhibited by Eqs. (14b), (19a), and (19b) for the number of repeatedly branching vessels of a space-filling embedding fractal model [15, 55] in the systemic arterial network proposed by West et al. [87], both β and γ resulted in $N^{-1/3}$ [87]. So when N is set at 2, as in our bifurcation model [15, 36, 41, 57, 61, 66], both β and γ should theoretically be 0.79 ($= 2^{-1/3}$), which is in good agreement with our results of β in systemic and pulmonary vasculature with severe PH. In our analysis, γ under $x = 3$ was estimated as 0.83 (systemic) or 0.85 (pulmonary Gr. 5, 6), which was only 4.5–7.1% larger than 0.79 (Table 4).

In order to assess the validity of n_p, which is the function of x, as indicated in Eq. (21), in our control group, we selected those pulmonary vessels with a radius of 100 μm among controls first and then compared the estimated n_p in terms of "order" with the reported morphometric counterparts (Table 6). The order rule, inversely numbering arteries from the most peripheral precapillary arteriole backward to the most proximal artery, has been widely applied to vascular morphometry [33, 36, 61]. Our model-derived n_p for the resistive area of the peripheral pulmonary vasculature in normal controls exceeded its morphometrically determined counterparts in the literature by 1 or 2 (Table 6).

Our results of $\tilde{n}_p$ shown in Table 4 suggested that the first resistive generation shifts by 3 ($\approx 11.0 - 8.3$) orders proximal in severe PH. This was consistent with the input impedance study in which the main reflection point of pulmonary artery pressure wave shifts more proximally in PH than in normal situations [4, 32].

Our β_p was in good agreement with the model analysis of Dawson et al. with $N_p = 2$, where their β_p resulted in 0.77 [12]. Yen et al. reported that N_p, β_p, and γ_p were 3.58, 0.58, and 0.55, respectively, in a cat's pulmonary arterial tree [90].

Table 6. Comparison of our model-derived estimates in our control group for generation, order, and number of vessels with pertinent morphometric data in the literature.

	Radius [μm]	Generation	Order	Number of vessels	Reference
Systemic					
Dog, 20 kg, whole arterial tree	75			1.1×10^5	[61]
	4*			$2.7 \times 10^{9*}$	
Dog, mesenteric artery	96	(3)	(4‡)	6.1×10^2	[75]
	11	(6)	(1‡)	1.3×10^6	
Our model, human, 15.7 (5.4–66.6) kg	100	1	11	$4.0\ (0.8–11.6) \times 10^4$	[63]
	10	11	1	$4.9\ (1.0–14.2) \times 10^7$	
Pulmonary					
Human, 112 ± 13 kg	110 ± 15	1	6	2.85×10^5	[36]
	10 ± 1	6	1	5.12×10^7	
Human, 32-years-old female	112	1	7	5.23×10^4	[76]
	10.5	6	2	1.27×10^7	
Human, 56-years-old male	112	1	7	5.81×10^4	[33]
	10.5	6	2	2.03×10^7	
Cat, 3.9–5.9 kg	96	1	5	2.93×10^3	[95]
	12	5	1	3.00×10^5	
Our model, human, 15.7 (5.4–66.6) kg	100	1	8	$3.6\ (0.6–19.0) \times 10^5$	[63]
	10	8	1	$5.5\ (0.9–29.6) \times 10^7$	

* Represents data of capillary. ‡ represents 'rank' in original paper. The number of rank is not exactly corresponding to order. The 'order' is the rule of reversely numbering arteries from the most peripheral terminal arteriole backward to the most proximal artery [33, 36, 76, 95]. Number of vessels in our model is presented as median with range. Table 6 was cited from ref. [64] after modification.

Combining the results of $\tilde{n}_p$ with β_p, we also interpreted that the radius of the 8th order vessel corresponded to approximately 50 μm in Gr. 5 and 6 because bifurcations through 3 generations yielded a 0.79^3 (= 0.49) times smaller radius than in controls. Thus, the partial resistance of an arterial tree distal to the 8th order was estimated to be 2.1 (= 6.2/2.9) times higher in Gr. 6 than in controls (Table 4). These results of controls and Gr. 6 are presented in Figures 17 and 18 as a schematic illustrations of vessel diameter and length within a single pulmonary unit resistive arterial tree in the case of BL = 1.2 m. Hence, the overall structural aspect in in vivo humans, as expected by our model in PH, renders the unit arterial tree much slenderer and 1.3 (= 4.0/3.0) times elongated in Gr. 6 than in controls (Figs. 17 and 18). These effects might be well accounted for by *in vivo* vasoconstriction due to medial hypertrophy in resistive arterial trees [31, 37, 59, 69].

Michel et al. reported the importance of early pathogenic changes exists in the pulmonary arterial vasoconstriction in L-R shunt lungs, which they examined using the arterial hyperreactivity to serotonin in an L-R shunted canine lobe at 7–20 months after surgical shunt operation [59]. However, they observed no significant histological differences in medial muscle thickness or the muscularization into smaller arteries between the shunt and control lobes in dogs.

Bergel et al. reported that the main reflecting sites moved to a more proximal site due to the pulmonary arterial vasoconstriction by serotonin in an impedance study of the pulmonary pressure wave velocity with anesthetized dogs in vivo [3]. They speculated that it might be caused by a 50% reduction in the distance to the major reflecting site, doubling of wave velocity, or by appropriate combination of the two effects.

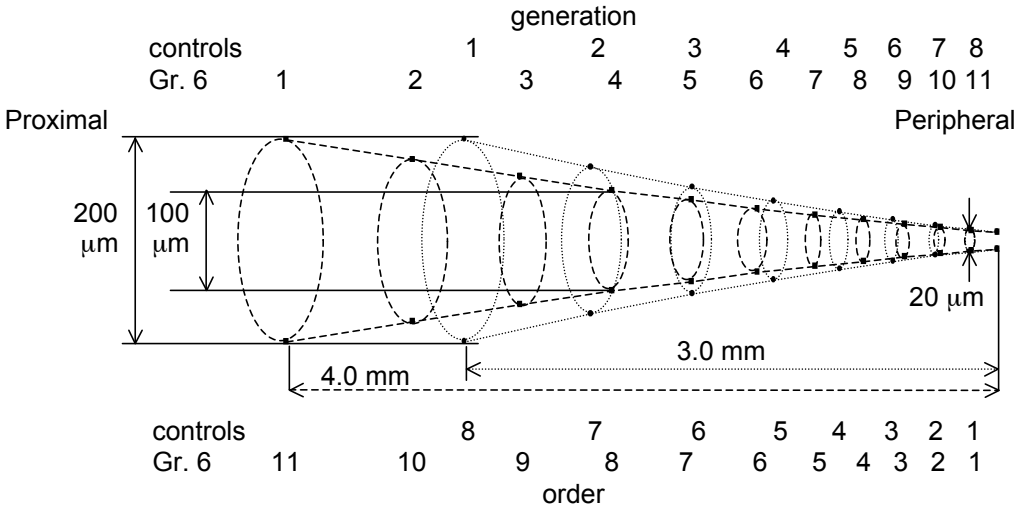

Figure 17. The schematic illustration indicates vessel radius and length of each generation of a unit resistive pulmonary arterial tree for either control (dotted lines) or Gr. 6 (dashed lines) for *BL* = 1.2 m; *BL*, body length; Gr., group. This figure was cited from ref. [63].

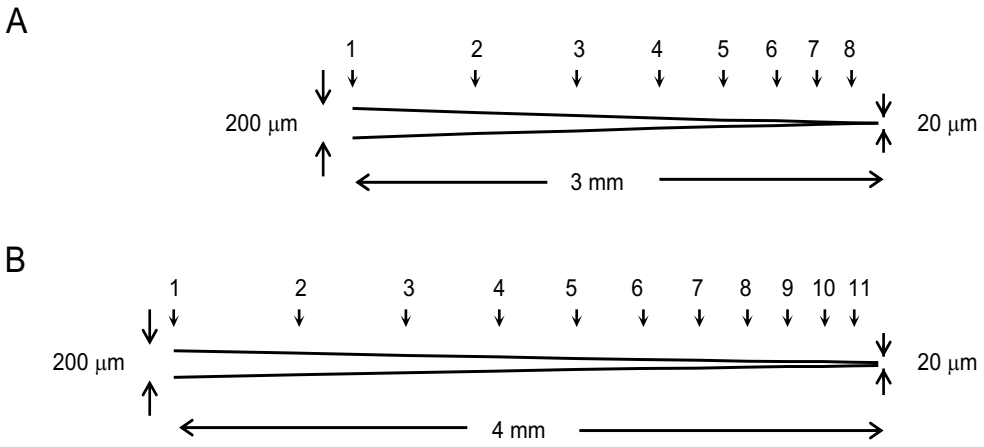

Figure 18. Separated lateral views of Figure 15 were drawn into control (**A**) and the Gr. 6 with the severest pulmonary hypertension (**B**) in our data for *BL* = 1.2 m similarly with indicators of each generation of a unit resistive pulmonary arterial tree; *BL*, body length. Figures were cited from ref. [64].

4.4. Numbers of peripheral arterial vessels.

4.4.1. Systemic arteries.

Estimated $N_{1\text{-s}}$ and $N_{n\text{-s}}$ were in good agreement with corresponding counterparts of canine morphometric data [61, 75] as the best available substitution for direct comparison because no pertinent morphometric data in human are available (Table 6).

4.4.2. Pulmonary arteries.

Controls. The estimated $N_{1\text{-p}}$ and $N_{n\text{-p}}$ in controls were also compared with published data of vessel numbers reported with their radius near 100 μm ($N_{1\text{-p}}$), and to those of precapillary arteriole equivalents ($N_{n\text{-p}}$), as shown in Table 6. Both $N_{1\text{-p}}$ and $N_{n\text{-p}}$ in controls were in good agreement with pertinent direct morphometric data in the literature [33, 36, 76].

Thus, our theoretical model gives good simulation results regarding the number of unit resistive arterial trees in normal controls, both pulmonary and systemic.

L-R shunt. A marked reduction in parallel $N_{1\text{-p}}$ (Fig. 16) results mainly from the more proximal involvement of arteries in the resistive arterial tree as a consequence of the slenderization and elongation of each component arteriole (Figs. 17 and 18), which in turn contributes to the substantial increase in pulmonary vascular resistance. $N_{w\text{-p}}$, on the other hand, reflects the peripheral pulmonary vascularity as a whole, because it represents the total number of component arteries in the peripheral resistive vascular network, as expressed in Eq. (25), and it was actually reduced in number substantially against P_{mpa} (Fig. 16). $N_{1\text{-p}}/BSA$ and $N_{w\text{-p}}/BSA$ in severe PH in our model may well explain the disturbed development in the number of intra-acinar arteries in VSD patients with severe PH in the literature [31, 69, 70].

4.4.3. Comparison of changes in the number and size of intra-acinar arteries due to L-R shunt between our prediction and histological data in the literature.

In relation to the reduced number and diminished radius size of acinar arteries, we tried to compare our results with these histopathological changes quantitatively reported in previous reports (Table 7).

Hislop et al. [31] and Rabinovitch et al. [70] examined the reduced number of intra-acinar arteries in patients with L-R shunt with PH through necropsy and biopsy, respectively, by measuring the alveolar artery ratio. Two studies reported that they did not observe significant changes in the number of alveoli between L-R shunted patients and controls, concluding that pulmonary high flow and induced PH would not have disturbed the development of alveoli after birth [31, 69, 70].

Ghorishi et al. reported that their shunt model in lambs displayed 1.5 to 2 times larger numbers of terminal arterioles and smaller pulmonary resistance than controls, presenting in their Figures 4B and 5, respectively, describing that these results did not reflect the reported properties of human subjects and other species [17]. They discussed that these paradoxical results may have been attributed to the isolated lung casts at 8 weeks after birth, genotypic variation and heterogeneity within a population of individuals and between species.

Table 7. Comparison among histopathological reports and our results.

Histology of intra acinar arteries (radius 10 – 100 μm)	Hislop et al. [31]	Rabinovitch et al. [70]	Our model [63]
Subject/Method	Human/Necropsy	Human/Biopsy	Human/Model analysis*
n	1	5	23
Corresponding PVR	4.6	3.5 – 10	6.8 ± 3.2
Decreased number of arteries	1/3†	1/5 – 1/8†	1/9
Radius compared to controls	—	2/3 – 1/2	-22%‡

n, the number of patients; PVR, pulmonary vascular resistance [mmHg·min·m^2/L]; *, data from our group 6; †, reversed data from the alveolar artery ratio, in which the number of alveoli was not changed for the age in comparison to controls in the literature [31, 70]; ‡, the estimated reduction in radius in Gr. 6 at the point of the beginning of the 1st generation in the controls [Fig. 17].

4.5. Clinical benefits supposed by these changes in the pulmonary arterial system due to the L-R shunt

The pathophysiological changes producing PH are desirable in some respects and include certain benefits. The vasoconstriction and suppressed development of intra-acinar arteries might play an important part in impeding further high flow, pulmonary edema, and capillary damage by restricting the increment of Q_p, because pulmonary capillaries are a crucial and delicate region in the lung to exchange gases. Furthermore, these adjustments to PH in peripheral pulmonary arteries lead to decreasing the preload of the left ventricle, which is the most important pump in the living body. The systemic circulation must remain stable in spite of increased pressure load to the right ventricle and peripheral pulmonary arteries. It is needless to say that the long-term pressure load to peripheral pulmonary arteries causes irreversible lesions of intimal thickening [27, 69, 89, 90], thrombosis, and vasculitis [27, 59, 69, 84], which hamper the long-term prognosis of life. However, without these adjustments in pulmonary resistive arteries the short-term survival can be jeopardized because of lethal pulmonary edema and severe congestive heart failure.

4.6. Verification of the ratio between $\Delta P_{prox\text{-}P}$ and $\Delta P_{peri\text{-}P}$ in our model analyses.

The ratio of 1:6 between $\Delta P_{\text{prox-P}}$ and $\Delta P_{\text{peri-P}}$ reported by Bhattacharya et al. [6] was partially verified by our own catheter data. However, the basic parameters of x, β, and γ are not influenced by the ratio because this ratio does not change the regression slope (A) by Eqs. (18), (19a), and (26) to (29). We analyzed our hemodynamic data of P_{mpa} in relation to the mean pressure of the 1st branch daughter artery ($P_{\text{1st-pbr}}$), as shown in Table 7, adopting the higher pressure between the two (left or right) daughter branches as $P_{\text{1st-pbr}}$. The pressure drop through the 1st branching ($\Delta P_{\text{1st-pbr}}$) was given by ($P_{\text{mpa}} - P_{\text{1st-pbr}}$). The mean generations included in proximal large arteries ($\Delta\tilde{n}$, real number) in each group were estimated by subtracting $\tilde{n}$ from the total generations of the whole pulmonary arterial tree (=15) using the data in ref. [36] and our Table 4. If the same ratio of $\Delta P_{\text{1st-pbr}}/(P_{\text{mpa}} - P_{\text{paw}})$ is conserved as the pressure drop ratio through all the successively lower bifurcations as in the mode of a functional fractal, then these next two equations should hold true:

$$\Delta P_{\text{prox-p}}/(P_{\text{mpa}} - P_{\text{paw}}) = 1 - \{1 - \Delta P_{\text{1st-pbr}}/(P_{\text{mpa}} - P_{\text{paw}})\}^{\Delta\tilde{n}\text{-}1} \text{ and}$$

$$\Delta P_{\text{peri-p}}/(P_{\text{mpa}} - P_{\text{paw}}) = \{1 - \Delta P_{\text{1st-pbr}}/(P_{\text{mpa}} - P_{\text{paw}})\}^{\Delta\tilde{n}\text{-}1} - \Delta P_{\text{cv-p}}/(P_{\text{mpa}} - P_{\text{paw}}).$$

From this simulation, the ratio of $\Delta P_{\text{peri-p}}$ to ($\Delta P_{\text{prox-p}} + \Delta P_{\text{peri-p}}$) in Gr. 2–6 was approximately 0.8, which was in good agreement with 6/7 (= 0.86) as assumed in our model in Section *2.1.* in the Methods [6], whereas those in the controls and Gr. 1 proved to be slightly lower than 6/7 (Table 7). Table 7 also indicates that the ratio of $\Delta P_{\text{peri-p}}$ to ($P_{\text{mpa}} - P_{\text{paw}}$) increases with the severity of PH, which suggests that the peripheral resistive arterial bed is exposed to more mechanical stress [59]. In addition, the multiplier 6/7 for the total pulmonary arterial pressure gradient in the estimation of $\Delta P_{\text{peri-p}}$ does not influence the slope A_{P} per se of the $\ln Q_{\text{p}}$ vs. $\ln(R_{\text{peri-p}}/BL)$ relationship by Eqs. (26) to (29). x_{p} is computed independently of the multiplier value and represents only the model structure of the peripheral arterial network itself.

Table 8. Estimation of pulmonary pressure gradient distributions through proximal arteries ($\Delta P_{\text{prox-p}}$), peripheral resistive arteries ($\Delta P_{\text{peri-p}}$), and capillaries and veins ($\Delta P_{\text{cv-p}}$).

Group	$\Delta\tilde{n}$	$\frac{\Delta P_{1\text{st}-\text{pbr}}}{P_{\text{mpa}}-P_{\text{paw}}}$	$\frac{\Delta P_{\text{prox}-\text{p}}}{P_{\text{mpa}}-P_{\text{paw}}}$	$\frac{\Delta P_{\text{peri}-\text{p}}}{P_{\text{mpa}}-P_{\text{paw}}}$	$\frac{\Delta P_{\text{cv}-\text{p}}}{P_{\text{mpa}}-P_{\text{paw}}}$	$\frac{\Delta P_{\text{peri}-\text{p}}}{\Delta P_{\text{prox}-\text{p}}+\Delta P_{\text{peri}-\text{p}}}$
Controls	6.7	0.038	0.20	0.30	0.50	0.60
1	5.0	0.053	0.20	0.39	0.41	0.67
2	5.0	0.042	0.16	0.57	0.27	0.78
3	5.1	0.045	0.17	0.65	0.18	0.79
4	4.6	0.065	0.21	0.68	0.11	0.76
5	4.3	0.057	0.18	0.74	0.08	0.81
6	4.0	0.069	0.19	0.74	0.07	0.79

$\Delta\tilde{n}$ stands for mean generations from the most proximal to the arteries immediately before the beginning of intra-acinar arteries in each group, estimated as the gap between the order of the main pulmonary artery from the data of ref. [36] and $\tilde{n}$ in Table 4. P_{mpa} and P_{paw} represent the mean pressures of main pulmonary artery and pulmonary artery wedge, respectively. $\Delta P_{\text{1st-pbr}}$ designates the mean pressure gradient between the main pulmonary artery and its 1st branch. Our model premises $\frac{\Delta P_{\text{prox}-\text{p}}}{P_{\text{mpa}}-P_{\text{paw}}} + \frac{\Delta P_{\text{peri}-\text{p}}}{P_{\text{mpa}}-P_{\text{paw}}} + \frac{\Delta P_{\text{cv}-\text{p}}}{P_{\text{mpa}}-P_{\text{paw}}} = 1.0$. Table 8 was cited from ref. [63].

4.7. Fåhraeus–Lindqvist effect: one of the non-Newtonian effects

The Fåhraeus–Lindqvist effect [13, 26, 39, 66] also does not influence x (or A), but affects $G(n)$ (or B), as Eqs. (14b) and (19b) indicate. This effect on our controls produced -11.0% $R_{\text{peri-p}}$, which resulted in only -0.73 mmHg P_{mpa}. This is not too meaningful in physiological pulmonary circulation, as Dawson indicates [12], but this effect leads to a significant reduction of -21.0% in $R_{\text{peri-p}}$ of Gr. 6 and -16% in $R_{\text{peri-s}}$ in all patients. Thus, the Fåhraeus–Lindqvist effect plays an important role in alleviating afterload on the heart in these high resistance circumstances.

4.8. Theoretical examinations of changes in x from 2 to 3

4.8.1. The maximal blood flow hypothesis

From the standpoint of seeking the condition for maximal flow through the vessel, we can rearrange Eq. (2), $C = \left(\frac{8\mu l}{\pi r^4}\right) q^2 + K\pi r^2 l$, to express q as a function of r, rewriting q as $q(r)$. Eq. (2) was then converted as follows:

$$q(r) = \left\{\frac{\pi r^4}{8\mu l}(C - \pi r^2 l)\right\}^{1/2}, \ 0 < r < \left(\frac{E}{K\pi l}\right)^{1/2}. \tag{30}$$

Differentiating $q(r)$ with respect to r in Eq. (30) reveals that $q(r)$ reaches its maximum at $\partial q/\partial r = 0$, where $q(r)$ is again proportional to the cube of r (Fig. 19). Therefore, $x = 3$ can also be considered to functionally represent maximal blood flow transportability, and indicate the *in vivo* structural law of the bifurcation in this condition with Eqs. (8), (9) and (10).

Our results reflect the overall flow-dependent adaptive changes in arterial performance from the cross-sectional area-preserving or r^2 mode ($x \approx 2$) to the more hyperdynamic r^3 mode ($x \approx 3$) as a consequence of the forcefully increased flow and the resultant high arterial pressure.

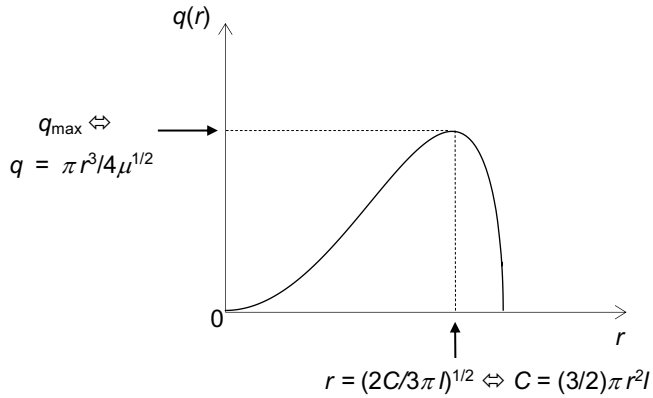

Figure 19. The curve of Eq. (30) was illustrated with the *q*-*r* relationship. Maximum value of q was given by $\pi r^3/4\mu^{1/2}$ when $r = (2C/3\pi l)^{1/3}$, where q was proportional to the r^3 which is equal to Murray's law: Substituting $C = (3/2)\pi r^2 l$ into Eq. (30) produces $q = \pi r^3/4\mu^{1/2}$.

4.8.2. The least energy principle

We designed the energy function for a single artery and designated it E, which represents the whole energy needed to drive and transport blood, and maintain both the vessel and the blood, in our recent article [65]. Blood flow was treated as a viscous incompressible Newtonian fluid for simplicity. This analysis did not take into account non-Newtonian effects and energy dissipations due to either turbulence or arterial ramifications.

Time average or the mean of kinetic, pressure, and metabolic and thermal energies of blood flow are defined as U_{K}, U_{P}, and U_{M}, respectively. Mean losses of kinetic, pressure, and metabolic and thermal energies through the vessel per unit time are represented as ΔU_{K}, ΔU_{P}, and ΔU_{M}, respectively. Energy dissipation due to turbulence of blood flow was also not taken into consideration either in this model.

The energy conservation through this single artery is expressed as:

$$E - (\Delta U_{\mathrm{K}} + \Delta U_{\mathrm{P}} + \Delta U_{\mathrm{M}}) = U_{\mathrm{K}} + U_{\mathrm{P}} + U_{\mathrm{M}}.$$

Thus, we get:

$$E = (U_{\mathrm{K}} + \Delta U_{\mathrm{K}}) + (U_{\mathrm{P}} + \Delta U_{\mathrm{P}}) + (U_{\mathrm{M}} + \Delta U_{\mathrm{M}}): \tag{31}$$

The rigorous cost function C is definable in Eq. (31) by:

$$C = \Delta U_{\mathrm{K}} + \Delta U_{\mathrm{P}} + \Delta U_{\mathrm{M}}. \tag{32}$$

Minimizing E optimizes the arterial design of this model analysis, while minimizing C reaches Murray's law as a result.

4.8.2.1 Energy function for an elastic artery

The common factor in two small pressure-losing systems, proximal systemic arteries and whole pulmonary arteries, lies largely in the elasticity of the arterial wall [1, 12, 16, 18, 49, 61, 66, 68, 95].

The mean of the internal vessel radius and length over time and space in a single elastic artery are indicated as r and l, and the mean blood volume flow per unit time and the mean pressure over time and space are also represented as q and P, respectively. The pressure drop produced along the length of the vessel is expressed by ΔP.

Indicating the specific gravity of blood as ρ, the mean mass of blood volume flow per unit time is given by $\rho \times q$. The mean linear velocity v at the gravitational center of blood flow is given as $q/\pi r^2$. Thus, U_{K}, the kinetic energy of blood flow through the vessel per unit time, is expressed in Eq. (33):

$$U_{\mathrm{K}} = \frac{1}{2}\rho q v^2 = \frac{1}{2}\,\rho q \left(\frac{q}{\pi r^2}\right)^2. \tag{33}$$

In an elastic artery with a modicum of tapering, Bernoulli's effect provides an increase in U_{K}, which makes ΔU_{K} negative. U_{P} and ΔU_{P} are described as shown below [61]:

$$U_{\mathrm{P}} = Pq \text{ and} \tag{34}$$

$$\Delta U_{\mathrm{P}} = \Delta P q. \tag{35}$$

U_{M} is defined as the sum of the metabolic energy converted from the oxygen supply of arterial blood flow and genuine thermal energy in it:

$$U_{\mathrm{M}} = K' q, \tag{36}$$

where K' indicates the proportional coefficient of two elements including the equivalent metabolic energy of arterial oxygen volume [57, 65] and thermal energy in blood [65].

Furthermore, ΔU_{M} in this paper is defined again from Eq. (2) as:

$$\Delta U_{\mathrm{M}} = K\pi r^2 l. \tag{37}$$

This is as in Murray's [62] or Mayrovitz and Roy's equations [57]. However, the relationship between l vs. r of an arterial tree in a number of human organs has already been reported by Suwa and Takahashi [80], who indicated that l was a function of r using real numbers α and L in both systemic and pulmonary arteries as:

$$l = Lr^{\alpha}. \tag{38}$$

This empirical expression has been applied widely in arterial fractal models [12, 15, 39, 45, 67, 80, 87]. The morphologically estimated value of the exponent α centers around 1.0, ranging from 0.76 to 1.21, in various human systemic [39, 80] as well as mammalian pulmonary arteries [12, 80]. Simply assumed to be 1.0, it has generally been used and discussed in model studies [12, 15, 39, 45, 67, 80, 87]. Therefore, when we need to deal with α in this model analysis, α is set tentatively to 1.0 for the sake of simplicity and brevity. As a result, Eq. (37) was rewritten with Eq. (38) as:

$$\Delta U_{\mathrm{M}} = K\pi Lr^{2+\alpha}. \tag{39}$$

Substitution of Eqs. (33), (34), (35) (36), and (39) into Eq. (31) gives:

$$E = \frac{1}{2}\rho q\left(\frac{q}{\pi r^2}\right)^2 + \Delta U_{\mathrm{K}} + (P + \Delta P)q + K'q + K\pi Lr^{2+\alpha}. \tag{40}$$

Because Bernoulli's effect always guarantees reciprocal conversion between ΔU_{K} and ΔU_{P} as $\Delta U_{\mathrm{K}} + \Delta U_{\mathrm{P}} \approx 0$ throughout an elastic artery [5, 51, 52, 66], $\Delta U_{\mathrm{K}} + \Delta Pq \approx 0$ also holds true in Eq. (40).

In conclusion, Eq. (40) is rewritten with Bernoulli's effect as:

$$E = \frac{1}{2}\rho q\left(\frac{q}{\pi r^2}\right)^2 + Pq + K'q + K\pi Lr^{2+\alpha}. \tag{41}$$

We partially differentiated E with respect to r, and applied $\partial E/\partial r = 0$ to Eq. (41) (Fig. 20). Because $\partial E/\partial r = 0$ in Eq. (41) results in $2\rho q^3 = (2+\alpha)K\pi^3 Lr^{6+\alpha}$, it follows

$$q = \pi\left\{\left(\frac{2+\alpha}{2}\right)\frac{KL}{\rho}\right\}^{1/3} r^{2+\alpha/3}. \tag{42}$$

Hence, x was directly derived from Eqs. (3) and (42) as follows:

$$x = 2 + \frac{\alpha}{3}. \tag{43}$$

When α is assumed equal to 1.0, x is deduced as 2.33. Of course, $x = 2 + \alpha/3$ of Eq. (43) also retains its validity both structurally and functionally even in the case of more complex asymmetric ramifications by fractal theory.

4.8.2.2. Energy function for a rigid artery

The energy function E in Eq. (31) was also applied to the analysis of the optimal design of a rigid artery. U_K, U_P, U_M, and ΔU_M are similarly expressed as counterparts in Eqs. (33,) (34), (36), and (39), respectively. Because ΔU_P in a rigid artery is due to the friction between viscous blood flow and the arterial inner surface [66], Hagen–Poiseuille's equation was applied as presented in Eq. (1). Because there is no change in mean linear velocity through a rigid artery due to Hagen–Poiseuille's law, ΔU_K is equal to 0 in Eq. (31). By substituting Eq. (38) into Eq. (1) and using $\Delta P \cdot q = R_{cyl} \cdot q^2$ as ΔU_P, E of a rigid cylindrical artery is finalized as:

$$E = \frac{1}{2}\rho q\left(\frac{q}{\pi r^2}\right)^2 + Pq + \frac{8\mu L r^{\alpha}}{\pi r^4}q^2 + K'q + K\pi L r^{2+\alpha}. \tag{44}$$

As a consequence, this involves the addition of Hagen–Poiseuille's term in $\Delta P \cdot q$ to Eq. (41). Similarly, the optimal relationship between q and r was sought by $\partial E/\partial r = 0$ (Fig. 20).

$\partial E/\partial r = 0$ as applied to Eq. (44) gave:

$$\left(\frac{2}{2+\alpha}\right)\frac{\rho}{K\pi^3 L r^{\alpha}}q^3 + \left(\frac{4-\alpha}{2+\alpha}\right)\frac{8\mu}{K\pi^2}q^2 = r^6. \tag{45}$$

Letting q/r be f for convenience, x is given below in Eq. (46) by taking α as 1.0 only at the exponent in Eq. (45) (Appendix):

$$x \cong 2 + \frac{(\rho f/\pi\mu)+8(4-\alpha)L}{3(\rho f/\pi\mu)+8(4-\alpha)L}. \tag{46}$$

Using $v = q/\pi r^2$, $f = q/r$, and $D = 2r$, where D stands for the internal vessel diameter, Reynolds number (Re) is defined and rewritten as shown in next Eq. (47) [34, 66]:

$$Re = \frac{vD\rho}{\mu} = \frac{2\rho r v}{\mu} = \frac{2\rho q}{\pi\mu r} = \frac{2\rho f}{\pi\mu}. \tag{47}$$

Eliminating f in Eq. (46) using Eq. (47), we can express x with Re and L as:

$$x \cong 2 + \frac{\zeta}{3}, \text{ where } \zeta = \frac{Re+16(4-\alpha)L}{Re+16(4-\alpha)L/3}. \quad (48)$$

Eq. (48) indicates that mean x asymptotically approaches its upper limiting value of 3.00 at Re <10 and to its lower limiting value 7/3 = 2.33 at Re >10^4.

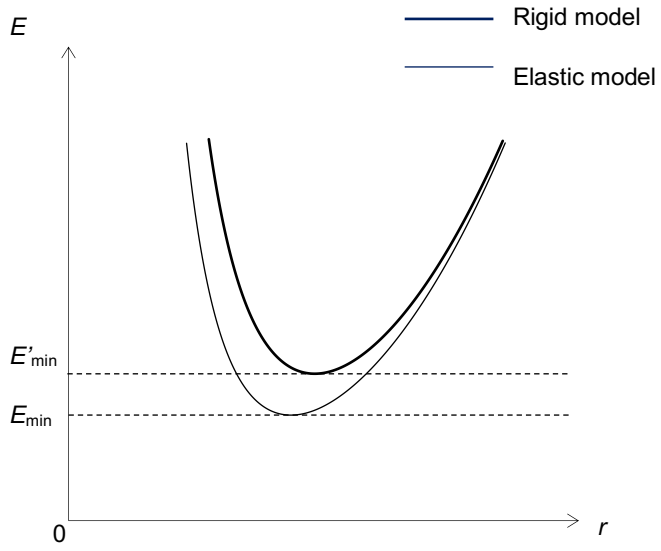

Figure 20. Schematic curves of E against r with the condition with constant q in the rigid and elastic arterial models when α is assumed to be 1.0, plotted by $E = ar^{-4} + br^{-3} + cr^3 + d$ and $E = ar^{-4} + cr^3 + d$ in the rigid and elastic models from Eq. (44) and (41), respectively; a, b, c, and d are real numbers. E_{min} and E'_{min} stand for the minimum values of E in the elastic and rigid models, respectively.

4.8.2.3. Verification of the least energy theory

Although we described the details previously [65], the theory was verified with published data in the literature in Figures 4 A and 4B as presented below in Figures 21A and 21B, respectively, in which reported and estimated mean x_s and x_p were plotted with the Eq. (48) and Eq. (43), respectively. Because the systemic arteries shift its wall properties from elastic ($x_s \approx 2$) proximal aorta to rigid peripheral ones ($x_s \approx 3$), while pulmonary arteries ($x_p \approx 2$) can be treated persistently with elastic arteries from proximal to peripheral regions [66].

As a result, these two equations well simulated the arrangement of x_s and x_p on the abscissa denoting the scale of radius and the corresponding *Re*, which was estimated using our previously reported methodology in ref. [65]. However, it is hard to explain the actual morphometric data of $x < 2$ or > 3, although those are rather extreme, observed in some particular states of normal mammalian vasculatures [3, 12, 48, 88] despite with our least energy model.

A

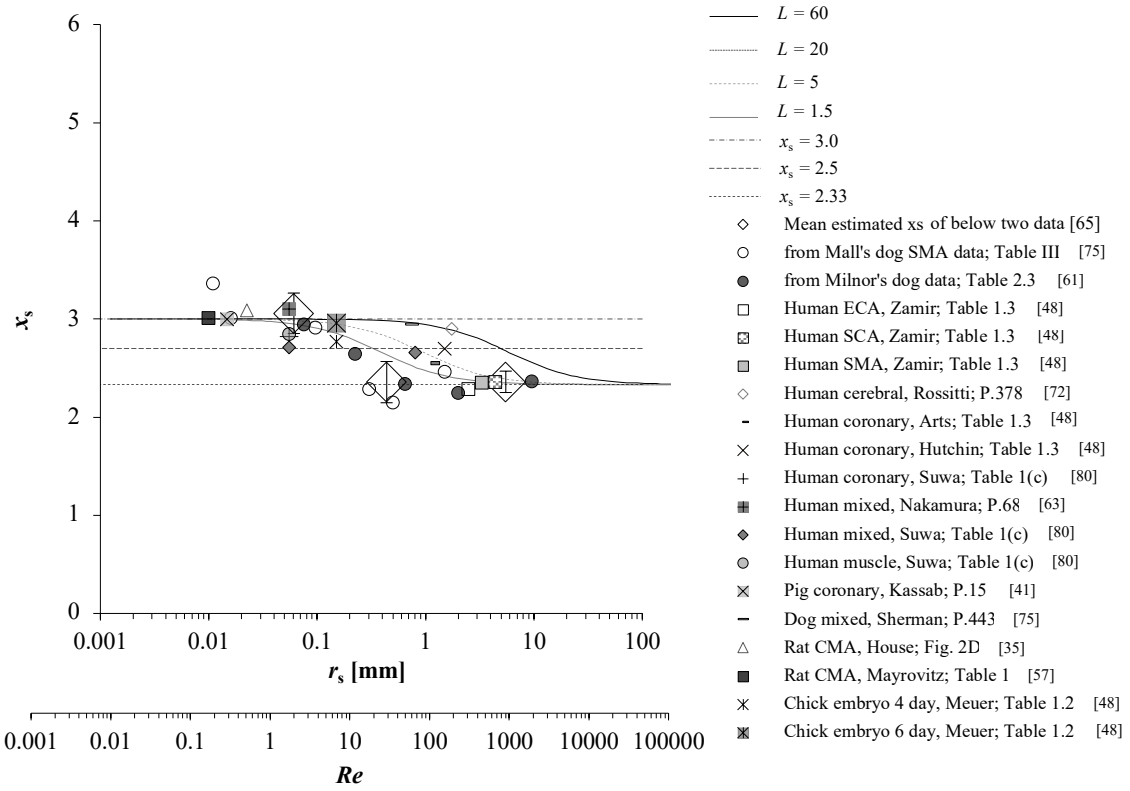
6
5
4
3
2
1
0
x_s
0.001
0.01
0.1
1
10
100
r_s [mm]
0.001
0.01
0.1
1
10
100
1000
10000
100000
Re
L = 60
L = 20
L = 5
L = 1.5
x_s = 3.0
x_s = 2.5
x_s = 2.33
Mean estimated xs of below two data [65]
from Mall's dog SMA data; Table III [75]
from Milnor's dog data; Table 2.3 [61]
Human ECA, Zamir; Table 1.3 [48]
Human SCA, Zamir; Table 1.3 [48]
Human SMA, Zamir; Table 1.3 [48]
Human cerebral, Rossitti; P.378 [72]
Human coronary, Arts; Table 1.3 [48]
Human coronary, Hutchin; Table 1.3 [48]
Human coronary, Suwa; Table 1(c) [80]
Human mixed, Nakamura; P.68 [63]
Human mixed, Suwa; Table 1(c) [80]
Human muscle, Suwa; Table 1(c) [80]
Pig coronary, Kassab; P.15 [41]
Dog mixed, Sherman; P.443 [75]
Rat CMA, House; Fig. 2D [35]
Rat CMA, Mayrovitz; Table 1 [57]
Chick embryo 4 day, Meuer; Table 1.2 [48]
Chick embryo 6 day, Meuer; Table 1.2 [48]

B

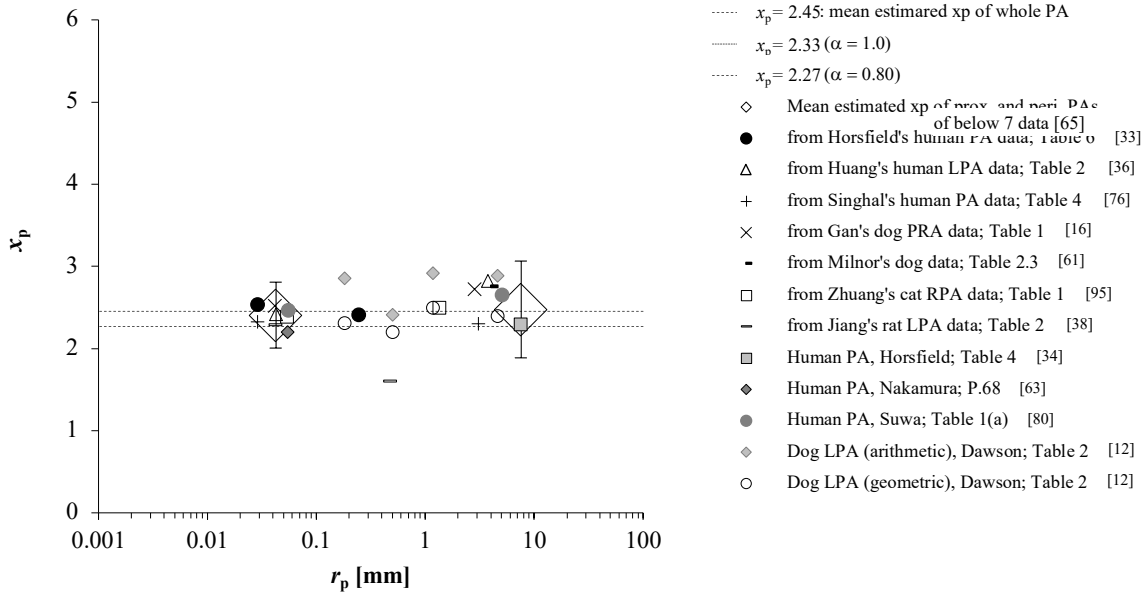
6
5
4
3
2
1
0
x_p
0.001
0.01
0.1
1
10
100
r_p [mm]
x_p= 2.45: mean estimared xp of whole PA
x_p= 2.33 (α = 1.0)
x_p= 2.27 (α = 0.80)
Mean estimated xp of prox. and peri. PAs of below 7 data [65]
from Horsfield's human PA data; Table 6 [33]
from Huang's human LPA data; Table 2 [36]
from Singhal's human PA data; Table 4 [76]
from Gan's dog PRA data; Table 1 [16]
from Milnor's dog data; Table 2.3 [61]
from Zhuang's cat RPA data; Table 1 [95]
from Jiang's rat LPA data; Table 2 [38]
Human PA, Horsfield; Table 4 [34]
Human PA, Nakamura; P.68 [63]
Human PA, Suwa; Table 1(a) [80]
Dog LPA (arithmetic), Dawson; Table 2 [12]
Dog LPA (geometric), Dawson; Table 2 [12]

Figure 21. A. Comparison between theoretical x from our rigid arterial model and morphometric x_s. The model-derived optimal relationship between the radius exponent x vs. Reynolds number (Re) in a rigid cylindrical artery was also plotted as curves based on Eq. (48), which shifted to the right with the increment of L. L represents the proportional coefficient of the vessel length-radius relationship in Eq. (38). Both reported mean x_s in the literature [36, 41, 48, 57, 63, 72, 80] and those estimated from two previous canine studies [61, 63, 75] were plotted together against corresponding r_s. Mean and one standard deviation (SD) of the estimates were plotted with large rhombuses and outliers, respectively, at proximal (x_s, 2.36 ± 0.11; r_s, 5.5 mm, range 1.5–9.5 mm), intermediate (x_s, 2.36 ± 0.21; r_s, 0.44 mm, range 0.23–0.65 mm), and peripheral arterial regions (x_s, 3.06 ± 0.21; r_s, 0.06 mm, range 0.01–0.10 mm), where Mall's rank 4 (corresponding to our 5th generation) arterial data [75] were excluded as an outlier. CMA, ECA, SCA, and SMA indicate the cremaster muscle, external carotid, subclavian, and superior mesenteric arteries, respectively. **B.** Comparison between the elastic arterial model derived x and morphometric x_p. Means of both reported x_p in the literature [12, 34, 63, 79] and those estimated from published data sets [16, 34, 36, 38, 61, 76, 95] were similarly plotted together against r_p. Large rhombuses with outliers indicate the mean of estimated x_p with one SD at proximal (x_p, 2.48 ± 0.59; r_p, 0.67 mm, range 0.11–15 mm) and peripheral arterial regions (x_p, 2.41 ± 0.40; r_p, 0.06 mm, range 0.01–0.10 mm). PA, pulmonary arterial tree; LPA and RPA, left and right pulmonary arterial trees, respectively; prox., proximal; peri., peripheral. r, vessel radius, presented as the mid-point of the range because the mean and median were not reported in the literature; x, radius exponent, defined by in Eq. (8) or (10); s and p, systemic and pulmonary, respectively. Figures were cited from ref. [65] after modification.

Our elastic arterial model explains $x = 2.33$ by Bernoulli's effect, which holds true for a single elastic artery and/or valve [5, 51, 52] although the effect is not necessarily guaranteed through arterial ramifications. $x = 2.33$ has conventionally been explained by Uylings' theoretical prediction in the condition of *complete turbulence* in a rigid cylindrical vessel [82], which is one of the most influential theories [3, 34, 36, 67, 75]. However, it still remains controversial how to explain the radius exponent reported in proximal systemic arteries as well as in the whole pulmonary arterial tree by the presence of turbulence alone [8, 34, 66, 73]. Because the peak *Re* in human systemic and pulmonary arteries is estimated as < 2000, except for the region just above the aortic valve [2, 66], it conflicts with the presence of continuous turbulence. Horsfield and Woldenberg stated that turbulence by itself may not fully account for the coexistence of both $x_p = 2.3 \pm 0.1$ and $Re < 2000$ at the same time in the case of pulmonary arteries, where several more direct effects resulting from arterial wall elasticity should also intervene [34].

The result in our rigid arterial model led us to represent x with a novel function of Re and L as presented in Eq. (48). This equation provides the general solution of optimal x for various blood flow levels, involving both Murray's and Uylings' theories. First, Murray's $\partial C/\partial r = 0$ in Eq. (32) is a particular solution of $\partial E/\partial r = 0$ of Eqs. (31) and (44). The ratio of U_K over ΔU_P in Eq. (44) is proportional to Re when α is equal to 1.0:

$$\frac{U_K}{\Delta U_P} = \frac{(1/2)\rho q\left(q/\pi r^2\right)^2}{8\mu L r^{\alpha} q^2/\pi r^4} = \frac{\rho r v}{16\mu L} \propto Re. \tag{49}$$

Because the result of $\partial E/\partial r = 0$ in Eq. (44) approximates that of $\partial C/\partial r = 0$ in Eq. (2) in the condition where $U_K \ll \Delta U_P$ and Re becomes sufficiently low as shown in Eq. (49), x reaches 3.00, which Murray's law [62] eventually advocates. Moreover, Uylings' theory is another particular solution of $\partial E/\partial r = 0$ under $Re \to \infty$. E in Eq. (44) appears similar to Eq. (43) in inverse conditions of $\Delta U_P \ll U_K$, where Re rises sufficiently high as in Eq. (49), and x

approaches 2.33, which is compatible with what Uylings' model relates [75, 82]. The complete turbulence in Eq. (44) means that blood flow closely mimics the ideal fluid with Bernoulli's principle.

The concept of the optimality principle itself, however, cannot escape some limitations. First, the *in vivo* vascular system must meet multiple functional requirements that are not fully expressible in terms of mathematical optimality conditions. Secondly, there is no guarantee that the vascular system will attain a mathematically deduced optimal state: in other words, the actual vessel structure of a living body shows significant asymmetry and heterogeneity [3, 12, 21, 88].

4.9. Limitations.

Our design of the arterial tree was set with r_n at 10 mm for simplicity. This is a limitation of our model to reflect the actual variable arterioles precisely. However, if we permitted the model to freely shrink the terminal arterial radii below 5 μm or less, it might have exceeded the reversible level of the arterial remodeling response to PH because the progression of radius reduction may result in substantial irreversible intimal thickening, partial thrombosis, and vascular occlusion. We need to also consider the pathophysiological condition of the pulmonary arteriolar structure with r_n < 10 μm [69] ideally, because setting the boundary of resistive arteries as 10–100 μm in radius is arbitrary although these constrains were for simplicity of the calculation and the design of vascular model. However, the multifractal paradigm can consider the effective dimension between two arbitrary radii and calculate the effective dimension. In this regard, our model may not be unique as a different compartmental model over different diameter ranges and different network fractal dimensions may be possible to represent regional variations [17, 19, 94]. Consequently, to establish the veracity of our model predictions of adaptation in a structure-function sense, additional morphometric/stereological studies are needed.

Another limitation was the use of the data measured in special conditions, i.e. catheterization, in which all subjects were systemically anesthetized by medicines although their voluntary respiration was completely maintained with a monitoring system. Fick's method to evaluate the volume blood flow at cardiac catheterization causes measurement errors of about 10% [29]. In addition, the oxygen consumption used in this study derives from an estimate [54], not from an actual measurement on the spot. $\Delta P_{\text{cv-p}}$ is not measured precisely in individual patients. In addition, we did not carry out the post-operative study of cardiac catheterization whether x_{p} recovered from 3 to around 2 in patients in Gr. 5 and/or 6 after the

surgery. We did not perform this routinely because we confirmed the regression of their severe PH to a normal level through clinical evaluations after the surgery as described in section of *2.3.3*.

As mentioned previously, $\Delta P_{\text{peri-p}}/(\Delta P_{\text{prox-p}} + \Delta P_{\text{peri-p}})$ may not stay constant at 6/7 through different severities of PH, as suggested in Table 7. These assumptions might interfere, to some extent, with the final outcome of our simulation results. Our results, however, were quite satisfactory, consistent, and rationally acceptable. Despite these limitations, our model results demonstrate that peripheral arterial vessels in the systemic and pulmonary circulation remodel their dimensions, consistent with a multifractal paradigm of tree adaptation. This adaptive change is clinically relevant because it occurs in diagnosed states where PH was demonstrated to be reversible upon surgical intervention.

Thus, irrespective of the veracity of the current model to interpret PVR and its anatomical site of radius, length, and number, the magnitude and direction of change earmarked by our fractal dimension x, is anticipated to provide significant information that may delineate states of irreversibility, such as leading to severe PH, and the transition of L-R to R-L shunts (Eisenmenger syndrome), that might not be apparent in the measurement of PVR alone.

4.10. Conclusions

In conclusion, our model interpretation suggests that the pulmonary peripheral resistive arteries in question, exposed to an obligatory large L-R shunt and PH, are bound to increase their total resistance by suppressing the development of vessel number on one hand and radius reduction on the other due to vasoconstriction, and that blood flow through them cannot escape reaching its maximal condition ($x = 3$) in this reduced capacity of the peripheral vascular bed. These effects will prevent, tentatively at least, the critical area of pulmonary function from developing into the advanced stage of PVD and decrease the preload of the left ventricle at the same time. We consider that these adaptive changes of the peripheral pulmonary arterial bed may reflect another aspect of Murray's minimum work principle, that is the maximal blood flow condition, or the least energy principle, as evidenced in the systemic circulation here and in the literature [15, 35, 57, 65].

Our fractal/multifractal model is based upon several assumptions that require additional morphologic/stereological verification in order for its uniqueness to accurately account for the vessel adaptation hypothesis summarized in Figures 16-18 [63-65]. At the same time, our model predicts information about adaptation during a disease process and identifies what region and what morphological indicators to look for in understanding the PH process further. Consequently, further studies based on fractal/multifractal simulation, impedance identification and morphometric studies are needed in humans and animal models of the disease to link physiology to pathology.

Our theoretical analyses of the maximal blood flow conditions and the least energy principle might propose a considerable candidate as one of the optimal designs describing the relationship between blood flow and radius in vascular trees, possibly providing the applicability for designing the vascular structure in artificial organs, prosthetic vessels, and

artificial circuits.

Hitherto, although the vascular resistance has played an important role as a clinically measurable parameter of the vascular bed, consisting of the vessel number, vessel length, radius, and blood viscosity, it cannot display nor describe the details of the vascular structure by itself. The introduction of fractal theory into the vascular resistance makes it possible to first simulate and estimate the changes in mathematical elements and geographical features in the vascular branching structure.

4.11. Appendix

In condition with α = 1.0 at the exponent in Eq. (38), Eq. (45) can be transformed to:

$$\frac{2\rho}{(2+\alpha)K\pi^3 L}\cdot\frac{q^3}{r^3}+\frac{8(4-\alpha)\mu}{(2+\alpha)K\pi^2}\cdot\frac{q^2}{r^2}\cong r^4. \tag{A1}$$

Using a real number ε as a proportional coefficient, Eq. (10) is used again as:

$$q=\varepsilon r^x. \tag{A2}$$

f can be defined as:

$$f=\frac{q}{r}. \tag{A3}$$

This can be used as a method to calculate Eq. (A1), the equation is simplified as:

$$Af^3+Bf^2=r^4, \tag{A4}$$

$$\text{where } A=\frac{2\rho}{(2+\alpha)K\pi^3 L} \text{ and } B=\frac{8(4-\alpha)\mu}{(2+\alpha)K\pi^2}. \tag{A5}$$

To make the successive composite functions easier or clear-cut for differential calculus, we tentatively define g, y, and z as follows for convenience:

$$g=\ln f, \tag{A6}$$

$$y=\ln(Af^3+Bf^2), \text{ and} \tag{A7}$$

$$z=\frac{\partial y}{\partial g}, \text{ respectively.} \tag{A8}$$

Eqs. (A2), (A3), and (A6) give us:

$$g=\ln\varepsilon+(x-1)\ln r. \tag{A9}$$

Eqs. (A4) and (A7) lead eventually to:

$$y=4\ln r. \tag{A10}$$

Eliminating r in Eq. (A9) by Eq. (A10) yields:

$$g=\ln\varepsilon+(x-1)\frac{y}{4}. \tag{A11}$$

Partial differentiation of g in Eq. (A11) with respect to y and Eq. (A8) results in:

$$\frac{\partial g}{\partial y}=\frac{x-1}{4}=\frac{1}{z}. \tag{A12}$$

On the other hand, Eqs. (A6), (A7), and (A8) provide:

$$z = \frac{\partial y}{\partial g} = \frac{dy}{df} \cdot \frac{df}{dg} = \frac{3Af^2+2Bf}{Af^3+Bf^2} f = \frac{3Af+2B}{Af+B}. \quad \text{(A13)}$$

With Eqs. (A5), (A12), and (A13) we can describe x as:

$$x = 1 + \frac{4}{z} = 1 + \frac{4(Af+B)}{3Af+2B} = 2 + \frac{(\rho f/\pi\mu)+8(4-\alpha)L}{3(\rho f/\pi\mu)+8(4-\alpha)L}.$$

5. Acknowledgments

The author first acknowledges my research mentor, Dr. Shoichi Awa, former professor of Pediatrics at the School of Medicine at Kyorin University and professor emeritus of Kyorin University, for advising me in this study, providing me many profound discussions on the theoretical model and clinical data, and reviewing and revising the manuscript for publication as for my first (*J Theor Biol* 287 (2011) 64-73) and second (*Physiol Rep* 2 (2) (2014) e00236) papers, and my chapter contribution (Advances in Medicine and Biology Vol. 52 (2012), Chapter VIII; pp. 219-239).

Secondly, the author would like to sincerely thank Dr. Hitoshi Kato and Dr. Takashi Igarashi, then lecturer and professor of Pediatrics at the Graduate School of Medicine at the University of Tokyo, respectively, and present director and president of National Center for Child Health and Development, respectively, for providing me the opportunity to perform this study utilizing clinical data with a deep understanding the objectives of the study as directors of pediatric cardiology and pediatrics, respectively; Dr. Yoichi Ito, then assistant at the Department of Biostatistics at the University of Tokyo School of Public Health and present professor and director of the Research Center for Medical and Health Data Science, for advising on the statistical methodology for this study; Dr. Akira Kamiya, former professor of System Physiology at the Department of Biomedical Engineering at the Graduate School of Medicine at the University of Tokyo and professor emeritus of University of Tokyo, for advising on the methodology for the fractal vascular model; Dr. N. B. Basnet (Nepal), Dr. Yoshie Nakamura, Dr. Shinichi Naritaka, Dr. Yasuhiro Yogo, and Dr. Joji Ando for continued encouragement.

The author is indebted to the anonymous reviewer for his or her inspiring comments and

advice. This helped me to improve and finalize the content and introduce findings that otherwise might have escaped our observation.

Finally, the author deeply thanks Dr. Akira Oka, professor of Pediatrics at the Graduate School of Medicine at the University of Tokyo, for the supervision of this thesis.

This dissertation includes the author's above published articles with permission.

6. References

1. **Al-Tinawi A, Madden JA, Dawson CA, Linehan JH, Harder DR, Rickaby DA.** Distensibility of small arteries of the dog lung. *J Appl Physiol* 71: 1714–1722, 1991.
2. **Becu LM, Fontana RS, DuShane JW, Kirklin JW, Burchell HB, Edwards JE,** Anatomic and pathologic studies in ventricular septal defect. *Circulation* 14: 349-364, 1956
3. **Bennett SH, Eldridge MW, Zaghi D, Zaghi SE, Milstein JM, Goetzman BW.** Form and function of fetal and neonatal pulmonary arterial bifurcations. *Am J Physiol Heart Circ Physiol* 279: H3047–H3057, 2000.
4. **Bergel DH and Milnor WR.** Pulmonary vascular impedance in the dog. *Circ Res* 16: 401-415, 1965.
5. **Bermejo J, Antoranz JC, Burwash IG, Rojo-Álvarez JL, Moreno M, García-Fernández MA, Otto CM.** In-vivo analysis of the instantaneous transvalvular pressure difference-flow relationship in aortic valve stenosis: implications of unsteady fluid-dynamics for the clinical assessment of disease severity. *J Heart Valve Dis* 11: 557–566, 2002.
6. **Bhattacharya J and Staub NC.** Direct measurement of microvascular pressures in the isolated perfused dog lung. *Science* 210: 327–328, 1980.
7. **Brody JS, Stemmler EJ, DuBois AB.** Longitudinal distribution of vascular resistance in the pulmonary arteries, capillaries, and veins. *J Clin Invest* 47: 783-799, 1968.
8. **Caro CG, Pedley TJ, Schroter RC, Seed WA.** *The Mechanics of the Circulation*. Oxford, UK: Oxford University Press. pp. 45-69, 1978.
9. **Chaliki HP, Hurrell DG, Nishimura RA, Reinke RA, Appleton CP.** Pulmonary venous

pressure: relationship to pulmonary artery, pulmonary wedge, and left atrial pressure in normal, lightly sedated dogs. *Catheter Cardiovasc Interv* 56(3): 432-8, 2002.

10. **Chemla D, Castelain V, Hervé P, Lecarpentier Y, Brimioulle S.** Haemodynamic evaluation of pulmonary hypertension. *Eur Respir J* 20: 1314-31, 2002.
11. **Connolly DC, Kirklin JW, Wood EH.** The relationship between pulmonary artery wedge pressure and left atrial pressure in man. *Circ Res* 2(5): 434-40, 1954.
12. **Dawson CA, Krenz GS, Karau KL, Haworth ST, Hanger CC, Linehan JH.** Structure-function relationships in the pulmonary arterial tree. *J Appl Physiol* 86: 569–583, 1999.
13. **Fåhraeus R, Lindqvist T.** The viscosity of the blood in narrow capillary tubes. *Am J Physiol* 96: 562-568, 1931.
14. **Fowler NO, Westcott RN, Scott RC.** Normal pressure in the right heart and pulmonary artery. *Am Heart J* 46 (2): 264-267, 1953.
15. **Gafiychuk VV and Lubashevsky IA.** On the principles of the vascular network branching. *J Theor Biol* 212: 1-9, 2001.
16. **Gan RZ and Yen RT.** Vascular impedance analysis in dog lung with detailed morphometric and elasticity data. *J Appl Physiol* 77: 706–717, 1994.
17. **Ghorishi Z, Milstein JM, Poulain FR, Moon-Grady A, Tacy T, Bennett SH, Fineman JR, Eldridge MW,** Shear stress paradigm for peripheral fractal arterial network remodeling in lambs with pulmonary hypertension and increased pulmonary blood flow. *Am J Physiol Heart Circ Physiol* 292: H3006-H3018, 2007.
18. **Gow BS and Taylor MG.** Measurement of viscoelastic properties of arteries in the living dog. *Circ Res* 23: 111–122, 1968.
19. **Grasman J, Brascamp JW, Van Leeuwen JL, Van Putten B.** The Multifractal Structure of Arterial Trees. *J Theor Biol* 220: 75-82, 2003.

20. **Greenwood EM, Meyrick B, Steinhorn RH, Fineman JR, Black SM.** Alterations in TGF-β1 expression in lambs with increased pulmonary blood flow and pulmonary hypertension. *Am J Physiol Lung Cell Mol Physiol* 285: L209-L221, 2003.

21. **Griffith TM, Edwards DH.** Basal EDRF activity helps to keep the geometrical configuration of arterial bifurcations close to the Murray optimum. *J Theor Biol* 146: 545–573, 1990.

22. **Grifka RG.** Cardiac catheterization and angiography. In: H.D. Allen, D.J. Driscoll, R.E. Shaddy, T.F. Feltes (Eds.), *Moss and Adams' Heart Disease in Infants, Children, and Adolescents: Including the Fetus and Young Adult, seventh ed*. Lippincott Williams & Wilkins, Philadelphia. pp. 208-237, 2008.

23. **Guyton AC.** Pulmonary circulation; pulmonary edema; pleural fluid. In: *Textbook of Medical Physiology, eighth ed.* Philadelphia, PA: WB Saunders. pp. 414–421, 1991.

24. **Hakim TS, Michel RP, Chang HK.** Partitioning of pulmonary vascular resistance in dogs by arterial and venous occlusion. *J. Appl. Physiol.* 52: 710-715, 1982.

25. **Harris P, Heath D, Apostolopoulos A.** Extensibility of the pulmonary trunk in heart disease. *Brit heart J* 27: 660-666, 1965.

26. **Haynes RH.** Physical basis of the dependence of blood viscosity on tube radius. Am J Physiol 198: 1193-1200, 1960.

27. **Heath D and Edwards JE.** The pathology of hypertensive pulmonary vascular disease: A description of six grades of structural changes in the pulmonary arteries with special reference to congenital cardiac septal defects. *Circulation* 18: 533-547, 1958.

28. **Hill KD, Lim DS, Everett AD, Ivy DD, Moore JD.** Assessment of pulmonary hypertension in the pediatric catheterization laboratory: Current insights from the magic registry. *Catheter Cardiovasc Interv* 76: 865-873, 2010.

29. **Hillis LD, Firth BG, Winniford MD.** Analysis of factors affecting the variability of Fick versus indicator dilution measurements of cardiac output. *Am J Cardiol* 56: 764-768, 1985.

30. **Hislop A and Reid L.** Pulmonary arterial development during childhood: branching pattern and structure. *Thorax* 28: 129-135, 1973.

31. **Hislop A, Haworth SG, Shinebourrne EA, Reid L.** Quantitative structural analysis of pulmonary vessels in isolated ventricular septal defect in infancy. *Br Heart J* 37: 1014-1021, 1975.

32. **Hopkins RA, Hammon JW Jr., McHale PA, Smith PK, Anderson RW.** Pulmonary vascular impedance analysis of adaptation to chronically elevated blood flow in the awake dog. *Circ Res* 45: 267-274, 1979.

33. **Horsfield K.** Morphometry of the small arteries in man. *Circ Res* 42: 593-597: 1978.

34. **Horsfield K and Woldenberg MJ.** Diameters and cross-sectional areas of branches in the human pulmonary arterial tree. *Anat Rec* 223: 245-251, 1989.

35. **House SD and Lipowsky HH.** Microvascular hematocrit and red cell flux in rat cremaster muscle. *Am J Physiol* 252: H211-H222, 1987.

36. **Huang W, Yen RT, McLaurine M, Bledsoe G.** Morphometry of the human pulmonary vasculature. *J Appl Physiol* 81: 2123-2133, 1996.

37. **Hyman AL.** Pulmonary vasoconstriction due to nonocclusive distension of large pulmonary arteries in the dog. *Circ Res* 23: 401-413, 1968.

38. **Jiang ZL, Kassab GS, Fung YC.** Diameter-defined Strahter system and connectivity matrix of the pulmonary arterial tree. *J Appl Physiol,* 76: 882-892, 1994.

39. **Kamiya A and Takahashi T.** Quantitative assessments of morphological and functional properties of biological trees based on their fractal nature. *J Appl Physiol* 102: 2315-2323, 2007.

40. **Karau KL, Krenz GS, Dawson CA.** Branching exponent heterogeneity and wall shear stress distribution in vascular trees. *Am J Physiol Heart Circ Physiol* 280: H1256-H1263, 2001.

41. **Kassab GS and FungYC.** The pattern of coronary arteriolar bifurcations and the uniform shear hypothesis. *Ann Biomed Eng* 23: 13–20, 1995.

42. **Kassab GS.** Scaling laws of vascular trees: of form and function. *Am J Physiol Heart Circ Physiol* 290: H894-H903, 2006.

43. **Kirklin JW, Barrat-Boyes BG.** Ventricular septal defects. In: J.W. Kirklin, B.G. Barratt-Bayes (Eds.), *Cardiac surgery: morphology, diagnostic criteria, natural history, techniques, results and indications, second ed.* Churchill Livingstone, New York. pp. 749-824, 1993.

44. **Kitaoka H and Suki B.** Branching design of the bronchial tree based on a diameter-flow relationship. *J Appl Physiol* 82: 968-976, 1997.

45. **Kizilova NN.** Modeling of intraorgan arterial vasculature, I: Steady flow at low Reynolds numbers. *Biophysics* 51: 654–658, 2006.

46. **Kovacs G, Berghold A, Scheidl S, Olschewski H.** Pulmonary arterial pressure during rest and exercise in healthy subjects: a systematic review. *Eur Respir J* 34: 888–894, 2009.

47. **Kuczmarski RJ, Ogden CL, Grummer-Strawn LM, Flegal KM, Guo SS, Wei R, Mei Z, Curtin LR, Roche AF, Johnson CL.** CDC Growth Charts: United States. *Adv Data* 314: 1-27, 2000.

48. **LaBarbera M.** The design of fluid transport system: a comparative perspective. In: J.A. Bevan, G. Kaley, G.M. Rubanyi (Eds.), *Flow-Dependent Regulation of Vascular Function*. New York, NY: Oxford University Press. pp. 3–27, 1995.

49. **Learoyd BM, Taylor MG.** Alterations with age in the viscoelastic properties of human

arterial walls. *Circ Res* 18: 278–292, 1966.

50. **Lefèvre J.** Teleonomical optimization of a fractal model of the pulmonary arterial bed. J Theor Biol 102: 225-248, 1983.
51. **Lima CO, Sahn DJ, Valdez-Cruz LM, Allen HD, Goldberg SJ, Grenadier E, Barron JV.** Prediction of the severity of left ventricular outflow tract obstruction by quantitative two-dimensional echocardiographic Doppler studies. *Circulation* 68: 348–354, 1983.
52. **Lima CO, Sahn DJ, Valdez-Cruz LM, Goldberg SJ, Barron JV, Allen HD, Grenadier E.** Noninvasive prediction of transvalvular pressure gradient in patients with pulmonary stenosis by quantitative two-dimensional echocardiographic Doppler studies. *Circulation* 67: 866–871, 1983.
53. **Lipowsky HH.** Shear stress in the circulation. In: J.A. Bevan, G. Kaley, & G.M. Rubanyi (Eds.), *Flow-Dependent Regulation of Vascular Function*. New York, USA: Oxford University Press. pp. 28-45,1995.
54. **Lundell BP, Casas ML, Wallgren CG.** Oxygen consumption in infants and children during heart catheterization. *Pediatr Cardiol* 17: 207-213, 1996.
55. **Mandelbrot BB.** Trees and the diameter exponent. In: *The Fractal Geometry of Nature*. New York, USA: Freeman. pp. 156-166, 1983.
56. **Mandelbrot BB.** Multifractal Measures, Especially for Geophysicist. In: C.H. Sholz, B.B. Mandelbrot (Eds.), *Fractals in Geophysics*. Birkhäuser Verlag, Basel. pp. 5-42, 1989.
57. **Mayrovitz HN and Roy J.** Microvascular blood flow: evidence indicating a cubic dependence on arteriolar diameter. *Am J Physiol* 245: H1031-H1038, 1983.
58. **Meyer JU, Borgström P, Lindbom L, Intaglietta M.** Vasomotion patterns in skeletal muscle arterioles during changes in arterial pressure. *Microvasc Res* 35: 193–203, 1988.
59. **Michel RP, Hakim TS, Hanson RE, Dobell ARC, Keith F, Drinkwater D.** Distribution

of lung vascular resistance after chronic systemic-to-pulmonary shunts. *Am J Physiol* 249: H1106–H1113, 1985.

60. **Middleman S.** *Modeling Axisymmetric Flows: Dynamics of Films, Jets, and Drops*. San Diego, CA: Academic Press. pp. 1-42, 1995.
61. **Milnor WR.** *Hemodynamics*. Baltimore, MD: Williams & Wilkins. pp. 10-48, 1982.
62. **Murray CD.** The physiological principle of minimum work, In: The vascular system and the cost of blood volume. *Proc Natl Acad Sci USA* 12: 207–214, 1926.
63. **Nakamura Y, Awa S, Kato H, Ito YH, Kamiya A, Igarashi T.** Model combining hydrodynamics and fractal theory for analysis of in vivo peripheral pulmonary and systemic resistance of shunt cardiac defects. *J Theor Biol* 287: 64–73, 2011.
64. **Nakamura Y and Awa S.** Model methodology for analyzing peripheral arterial fractility from hemodynamic data. In: L.V. Berhardt (Ed.), *Advances in medicine and Biology. Volume 52.* NOVA Science Pub. Inc. New York. pp. 219-239, 2012.
65. **Nakamura Y and Awa S.** Radius exponent in elastic and rigid arterial models optimized by the least energy principle. *Physiol Rep* 2 (2): 2014, e00236. doi: 10.1002/phy2.236.
66. **Nichols WW and O'Rourke MF.** *McDonald's Blood Flow in Arteries: Theoretical, Experimental and Clinical Principles, fifth ed.* Hodder Arnold, London. pp.1-93 and 307-320, 2005.
67. **Olufsen MS, Peskin CS, Kim WY, Pedersen EM, Nadim A, Larsen J.** Numerical simulation and experimental validation of blood flow in arteries with structured-tree outflow conditions. *Ann Biomed Eng* 28: 1281–1299, 2000.
68. **Patel DJ, Schilder DP, Mallos AJ.** Mechanical properties and dimensions of the major pulmonary arteries. *J Appl Physiol* 15: 92–96, 1960.
69. **Rabinovitch M.** Pathophysiology of pulmonary hypertension. In: H.D. Allen, D.J.

Driscoll, R.E. Shaddy, T.F. Feltes (Eds.), *Moss and Adams' Heart Disease in Infants, Children, and Adolescents: Including the Fetus and Young Adult, seventh ed.* Lippincott Williams & Wilkins, Philadelphia. pp. 1322-1354, 2008.

70. **Rabinovitch M, Haworth SG, Castaneda AR, Nadas AS, Reid LM**. Lung biopsy in congenital Heart Disease: A morphometric approach to pulmonary vascular disease. *Circulation* 58: 1107-1122, 1978.
71. **Rippe B, Parker JC, Townsley MI, Mortillarro NA, Taylor AE.** Segmental vascular resistances and compliances in dog lung. *J Appl Physiol* 62: 1206-1215, 1987.
72. **Rossitti S and Löfgren J.** Vascular dimensions of the cerebral arteries follow the principle of minimum work. *Stroke* 24: 371–377, 1993.
73. **Roy AG and Woldenberg MJ.** A generalization of the optimal models of arterial branching. *Bull Math Biol* 44: 349–360, 1982.
74. **Schreiner W, Karch R. Neumann M, Neumann F, Roedler SM, Heinze G.** Heterogeneous perfusion is a consequence of uniform shear stress in optimized arterial tree models. *J Theor Biol* 220: 285-301, 2003.
75. **Sherman TF.** On connecting large vessels to small: the meaning of Murray's law. *J Gen Physiol* 78: 431–453, 1981.
76. **Singhal S, Henderson R, Horsfield K, Harding K, Cumming G.** Morphometry of the human pulmonary arterial tree. *Circ Res* 33: 190–197, 1973.
77. **Snyder GK and Sheafor BA.** Red blood cells: centerpiece in the evolution of vertebrate circulatory system. *Amer Zool* 39: 189-198, 1999.
78. **Soto B, Becker AE, Moulaert AJ, Lie JT, Anderson RH.** Classification of ventricular septal defects. *Br Heart J* 43: 332-343, 1980.
79. **Struijker-Boudier HAJ.** The burden of vascular disease in diabetes and hypertension:

from micro- to macrovascular disease—the “bad loop”. *Medicographia* 31: 251–256, 2009.

80. **Suwa N and Takahashi T.** *Morphological and Morphometrical Analysis of Circulation in Hypertension and Ischemic Kidney*. Munich, German: Urban & Schwarzenberg. pp. 1-40, 1971.

81. **Tatsuno K, Ando M, Takano A, Hatsune K, Konno S.** Diagnostic importance of aortography in conal ventricular-septal defect. *Am Heart J* 89: 171-177, 1975.

82. **Uylings HBM.** Optimization of diameters and bifurcation angles in lung and vascular tree structures. *Bull Math Biol* 39: 509–520, 1977.

83. **van der Feen DE, Bartelds B, Boer RA, Berger RMF.** Pulmonary arterial hypertension in congenital heart disease: translational opportunities to study the reversibility of pulmonary vascular disease. *Eur Heart J* 38: 2034-2040, 2017.

84. **Wagenvoort CA, Neufeld HN, DuShane JW, Edwards JE, Wagenvoort N.** The pulmonary arterial tree in ventricular septal defect: A quantitative study of anatomic features in fetuses, infants, and children. *Circulation* 23: 740-748, 1961.

85. **Wasserman SM and Topper JN.** Adaptation of the endothelium to fluid flow: in vitro analysis of gene expression and in vivo implications. *Vascular Medicine* 9: 35-45, 2004.

86. **Weibel ER.** Fractal geometry: a design principle for living organisms. *Am J Physiol* 261: L361-L369, 1991.

87. **West GB, Brown JH, Enquist BJ.** A general model for the origin of allometric scaling laws in biology. *Science* 276: 122-126, 1997.

88. **Woldenberg MJ.** Finding the optimal lengths for three branches at a junction. *J Theor Biol* 104: 301–318, 1983.

89. **Yamaki S, Endo M, Takahashi T.** Different grades of medial hypertrophy and intimal

changes in small pulmonary arteries among various types of congenital heart disease with pulmonary hypertension. *Tohoku J Exp Med* 182: 83-91, 1997.

90. **Yamaki S, Horiuchi T, Seino Y.** Quantitative analysis of pulmonary vascular disease in simple cardiac anomalies with the Down syndrome. *Am J Cardiol* 51: 1502-1506, 1983.
91. **Yen RT, Zhuang FY, Fung YC, Ho HH, Tremer H, Sobin SS.** Morphometry of cat's pulmonary arterial tree. *J Biomech Eng* 106: 131-136, 1984.
92. **Zamir M and Brown N.** Arterial branching in various parts of the cardiovascular system. *Am J Anat* 163: 295–307, 1982.
93. **Zamir M, Sinclair P, Wonnacott TH.** Relation between diameter and flow in major branches of the arch of the aorta. *J Biomech* 25: 1303–1310, 1992.
94. **Zamir M.** Fractal Dimensions and Multifractility in Vascular Branching. *J Theor Biol* 212: 183-190, 2001.
95. **Zhuang FY, Fung YC, Yen RT.** Analysis of blood flow in cat's lung with detailed anatomical and elasticity data. *J Appl Physiol* 55: 1341–1348, 1983.